UCLouvain

École polytechnique de Louvain

Handling of the fluid-structure interaction in an immersed lifting lines approach

Author: **Timothée Deschuyteneer**
Supervisors: **Philippe Chatelain, Paul Fisette**
Reader: **Grégoire Winckelmans**
Academic year 2018–2019
Master [120] in Mechanical Engineering

Remerciements

Ce travail marque la fin de cinq années d'étude et de projets pleines d'enrichissements et de rencontres à l'Ecole Polytechnique de Louvain-la-Neuve. Je tiens à remercier les personnes qui m'ont aidées et permises de mener à bien ce mémoire de fin d'étude.

Pour commencer, j'aimerais remercier le Professeur Philippe Châtelain, promoteur de ce mémoire, de m'avoir permis de réaliser ce travail. J'adresse particulièrement un tout grand merci à Denis-Gabriel Caprace et Victor Colognesi qui m'ont grandement aidé à réaliser ce mémoire. Leur patience, leurs précieux conseils ainsi que leur soutient moral m'ont grandement aidés tout au long du quadrimestre.

Enfin, je tiens à remercier mes proches qui m'ont soutenus à tous les stades de ce projet. Merci à ma mère pour sa relecture et ses corrections orthographiques, ainsi qu'à toute ma famille, mes amis et ma copine pour leur soutient.

Contents

Introduction **1**

1 Preliminary knowledge **3**
1.1 Flow solver . . . 4
1.1.1 The Vortex Particle-Mesh method . . . 4
1.1.2 Immersed lifting lines . . . 5
1.2 Multibody systems modeling and analyses . . . 6
1.2.1 Definitions and conventions . . . 6
1.2.2 Dynamical equations . . . 8
1.2.3 Symbolic generation . . . 9
1.2.4 Modal analysis . . . 9
1.3 Coupling of the flow and multibody solvers . . . 10
1.3.1 Coupling strategy . . . 10
1.3.2 Communication interface . . . 10

2 Methodology **13**
2.1 The finite segment approach . . . 14
2.1.1 Spring coefficients determination . . . 14
2.1.2 Validation 1 : uniform cantilever beam . . . 16
2.1.3 Validation 2 : NREL 5-MW wind turbine blade . . . 19
2.1.4 Conclusion . . . 22
2.2 Integrating the finite segment approach in the flow solver . . . 23
2.2.1 Modifications in the treatment of the mapping file . . . 23
2.2.2 From rigid segments to a curved line . . . 24

3 Results **29**
3.1 Validation 1 : Uniform rectangular wing . . . 29
3.1.1 Testing configuration . . . 29
3.1.2 Analytical solution . . . 30
3.1.3 Results . . . 31
3.2 Validation 2 : NREL 5-MW wind turbine blade . . . 31
3.2.1 Testing configuration . . . 32
3.2.2 Analytical solution . . . 33
3.2.3 Results . . . 34
3.3 Application : full NREL 5-MW blade in rotation . . . 35

Conclusion **39**

A Deformation of uniform cantilever beams **43**

B Assumed mode method for the bending of a non-uniform rotating blade **47**

Introduction

Wind turbines have been used for electricity production since the end of the 19th century, with the first windmill to generate electricity constructed by the American inventor Charles Brush in 1888 [1]. However, there was little interest in wind generation until the first oil shock in 1973. As a consequence of the sudden increase in oil prices, several countries launched researches aimed at developing cheap wind energy. Multiple designs were explored, but finally the simple architecture of the Danish wind turbine concept prevailed, with the classic three-bladed horizontal axis wind turbine (HAWT) (see figure 1) [2].

Figure 1: Three-bladed HAWT [3].

In addition to the oil prices, the awareness of the impact of CO_2 emissions generated by thermal energy sources on gobal warming boosted the development of wind turbines, leading to a quest for maximal power and effectiveness.

The power output of a wind turbine is given by

$$P = \frac{1}{2}\rho A U^3 C_p \tag{1}$$

where ρ is the density of air, A is the rotor swept area, U is the wind speed and C_p is the power coefficient. The power coefficient, limited to 0.593 according to Betz's law can be increased as a result of improvement of the design and the control. However, the major improvements are achieved by increasing the swept area and placing wind turbines on windy sites. This explains the continuous increase in rotor diameters and tower size (see Figure 2) and the development of offshore wind farms [2].

In operation, wind turbine blades may be submitted to high and unsteady loads. The unsteadiness is caused by multiple factors such as turbulence, wind shear, flow misalignment, tower shadow and gravity [2]. On the other side, to reduce the production cost and the weight

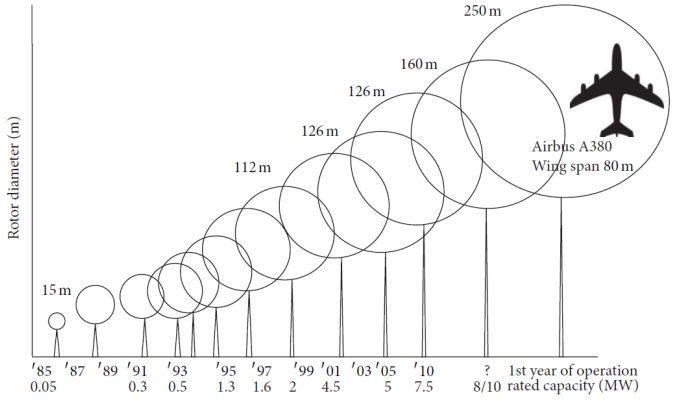

Figure 2: Three-bladed HAWT [3].

of the huge blades required for powerful wind turbines, their stiffness is limited, which implies that the blades can deform. These deformations also absorb the loads transmitted to the hub [4]. For accurate modelling of wind turbine performances and wake generation, it is important to take into account the flexibility of their blades. It is also important for design to determine aeroelastic instabilities and tip deflection to prevent rotor tips from colliding with the tower. Similar considerations apply to helicopter blades and aircraft wings.

However, modelling flexibility effects is a very arduous task. Indeed, it is necessary to make physical and geometrical approximations of a real flexible body (e.g., elastic linear behaviour, small deformations, ...) and the flexibility effects also greatly increase the number of variables required in the analysis and hence the computational cost.

The aim of this work is to account for the fluid-structure interaction and flexibility effects of lifting surfaces in a Vortex Particle-Mesh (VPM) method previously developed by the UCLouvain-TFL research team. This numerical tool has previously been coupled with a Multibody system dynamics solver, ROBOTRAN, that was also developed at UCLouvain. With the help of this coupling, the flexibility effects will be treated in an efficient and relatively precise way using finite segment modelling.

The present document describes the integration of the finite segment method in the Vortex Particle-Mesh method. In Chapter 1, a brief description is given of the two numerical tools used, as well as the coupling between them.

In Chapter 2, the method used to handle flexibility effects is presented. Firstly, it is described only in a Multibody systems context, and then the integration of the method in the flow solver is detailed. Finally, in Chapter 3, validation steps of the method are performed, followed by a brief application to a wind turbine blade.

Chapter 1

Preliminary knowledge

In this chapter, an overview of the numerical tools used for this work is presented. The numerical tools are (i) a Computational Fluid Dynamics (CFD) solver and (ii) a Multibody systems dynamics solver, both developed at the UCLouvain. The flow solver is a Vortex Particle-Mesh (VPM) method combined with immersed lifting lines, whose main strength is the tracking of vortical structures over very long times and distances (see figure 1.1). The second numerical tool, called ROBOTRAN, is symbolic software conceived to model and analyse Multibody systems.

The fundamental theoretical concepts of these tools are presented here. Their main features used in this work are also briefly described. For complete descriptions, the interested reader can refer to the bibliography.

Finally, the coupling mechanism between the aerodynamic solver and the Multibody systems dynamics solver is presented. The main role of this coupling is to simplify high degrees of freedom motions resolution in the flow solver.

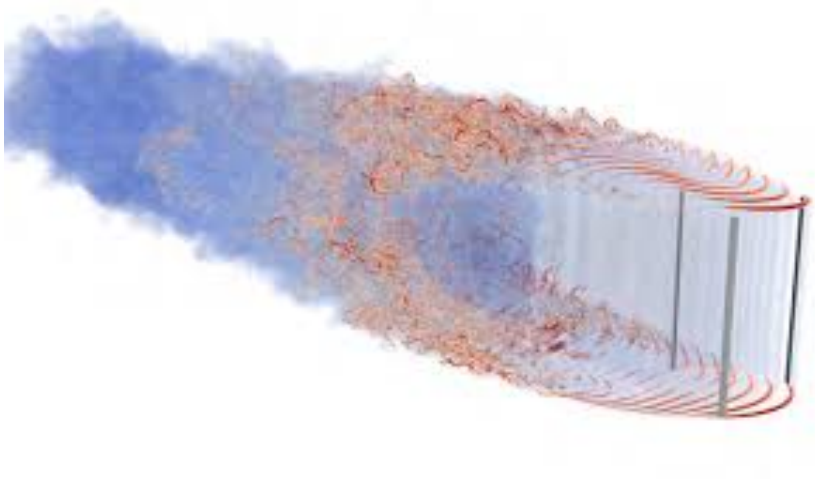

Figure 1.1: Illustration of the vortical structures generated by a vertical axis wind turbine simulated with the Vortex Particle-Mesh method [5].

1.1 Flow solver

Several numerical methods exist for predicting the flow structures generated by lifting surfaces, among which actuator line methods and free wake vortex lattice method. Vortex methods can be seen to combine the advantages of both methods. They treat vorticity in a Lagrangian manner and exploit its compactness. Unlike vortex lattice methods, they also allow the flow structures to evolve into a fully turbulent flow by solving the full Navier-Stokes equations.

The flow solver used here is a Vortex Particle-Mesh (VPM) method developed at UCL-TFL. It is a variant of the vortex methods, where the advection is treated with particles and a mesh handles all the other computationally intensive tasks. The solver offers high levels of accuracy and shows computational efficiency and high scalability on massively parallel architectures.

In this section, the vortex particle-mesh method is briefly explained, followed by the modeling of blades through immersed lifting lines. Other features and details concerning this method can be found in the related papers ([6], [7], [8] and [5]).

1.1.1 The Vortex Particle-Mesh method

The method relies on the Navier-Stokes equations for an incompressible flow in velocity ($\mathbf{u}$)-vorticity ($\boldsymbol{\omega} = \nabla \times \mathbf{u}$) formulation obtained by taking the curl of the momentum equation

$$\frac{D\boldsymbol{\omega}}{Dt} = (\boldsymbol{\omega} \cdot \nabla)\mathbf{u} + \nu \nabla^2 \boldsymbol{\omega} \tag{1.1}$$

$$\nabla \cdot \mathbf{u} = 0 \tag{1.2}$$

where $\frac{D}{Dt} = \frac{\partial}{\partial t} + \mathbf{u} \cdot \nabla$ denote the Lagrangian derivative and ν is the kinematic viscosity. The velocity field is recovered, after a Helmholtz decomposition $\mathbf{u} = \mathbf{U}_\infty + \mathbf{u}_\omega$, from the vorticity by solving the Poisson equation

$$\nabla^2 \mathbf{u}_\omega = -\nabla \times \boldsymbol{\omega}. \tag{1.3}$$

The vorticity field is discretized with particles, characterized by a position $\mathbf{x}_p$, a volume V_p and a strength $\boldsymbol{\alpha}_p = \int_{V_p} \boldsymbol{\omega} d\mathbf{x} \simeq \boldsymbol{\omega}_p V_p$. Those particles are convected by the flow field and their strength is modified to account for vortex stretching and diffusion

$$\frac{d\mathbf{x}_p}{dt} = \mathbf{u}(\mathbf{x_p}), \tag{1.4}$$

$$\frac{d\boldsymbol{\alpha}_p}{dt} = \int_{V_p} (\boldsymbol{\omega} \cdot \nabla)\mathbf{u} + \nu \nabla^2 \boldsymbol{\omega} d\mathbf{x} \tag{1.5}$$

$$\simeq \big((\boldsymbol{\omega} \cdot \nabla)\mathbf{u}(\mathbf{x}_p) + \nu \nabla^2 \boldsymbol{\omega}(\mathbf{x}_p)\big) V_p. \tag{1.6}$$

The Lagrangian description of convection (equation 1.4) allows for time steps of larger magnitudes than with Eulerian methods, which is one of the main advantages of this method. In order to prevent the depletion of some regions of the flow by the particles, resulting in the generation of spurious vortical structures, a remeshing is applied. This procedure maintains adaptivity while reducing the artificial dissipation of vortex methods. It consists in the periodic regularization of the particle set onto a mesh via a high-order interpolation

$$\boldsymbol{\alpha}_q = \sum_p \boldsymbol{\alpha}_p W\Big(\frac{\mathbf{x}_q - \mathbf{x}_p}{h}\Big) \tag{1.7}$$

where W is the interpolation kernel, $\mathbf{x}_q$ is on the mesh and h is the mesh spacing. To preserve the qualities of the method, the remeshing must be used as seldom as possible.

The mesh also improves the computational efficiency for evaluating the differential operators and obtaining an efficient solution of the Poisson equation using a Fourier solver (equation 1.3). Indeed, due to the interpolation of the particle quantities on the mesh, Finite Differences can be used to evaluate differential operators on the RHS of equation 1.5, and the result can then be interpolated back on the particle locations.

1.1.2 Immersed lifting lines

In this flow solver, slender lifting surfaces such as wings and blades are modeled by a lifting line model. Assuming a steady, two-dimensional flow airfoil, the lift $\mathbf{L}$, the relative velocity $\mathbf{V}_{rel}$ and the circulation Γ are related through the Kutta-Joukowski theorem

$$\mathbf{L} = \rho \mathbf{V}_{rel} \times \Gamma \hat{\mathbf{e}}_{\mathbf{\Gamma}} \tag{1.8}$$

where ρ is the air density and $\hat{\mathbf{e}}_{\mathbf{\Gamma}}$ is the vector tangent to the lifting line. With the same assumption of quasi-steady, two-dimensional flow, the 2D lift l can also be obtained from the relative velocity and the airfoil lift coefficient $C_l(\alpha)$

$$l = \frac{1}{2}\rho |\mathbf{V}_{rel} - (\mathbf{V}_{rel} \cdot \hat{\mathbf{e}}_{\mathbf{\Gamma}})\hat{\mathbf{e}}_{\mathbf{\Gamma}}|^2 \; c \; C_l(\alpha) \tag{1.9}$$

where c is the chord of the local airfoil. Equating the two expressions (1.8 and 1.9) provides the expression for instantaneous circulation Γ at a blade location

$$\Gamma = \frac{1}{2}|\mathbf{V}_{rel} - (\mathbf{V}_{rel} \cdot \hat{\mathbf{e}}_{\mathbf{\Gamma}})\hat{\mathbf{e}}_{\mathbf{\Gamma}}| C_l(\alpha). \tag{1.10}$$

The circulation can be related to vorticity by Stokes' theorem

$$\Gamma = \int_S \boldsymbol{\omega} \cdot \mathbf{n} dS \tag{1.11}$$

and because of the solenoidal property of vorticity $\nabla \cdot \boldsymbol{\omega} = 0$, streamwise and spanwise vorticities must be shed from the lifting line in order to account for the spanwise and temporal variations of the circulation, respectively.

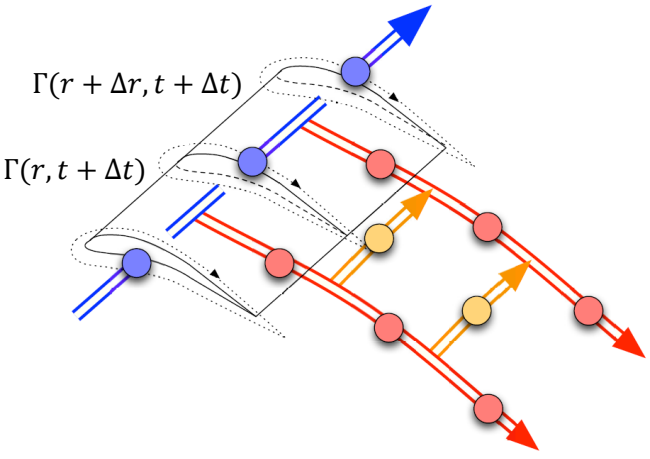

Figure 1.2: Discretization by particles of the bound and shed vorticities [9] .

To manage this shedding of vorticity, the lifting line is discretized in blade elements of size Δr close to the computational mesh size. At each time step, the bound vorticity is updated and, at the extremities of those blade elements, Lagrangian flow tracers are shed and advected by the flow over the course of the time step (see Figure 1.2). Those traces account for the

time and space variations of the circulation through a vortex sheet that is discretized by means of particles that are then immersed in the bulk vorticity through a particle-to-particle interpolation. This treatment of the vorticity sources is Lagrangian and allows large time steps.

In the previously described assumptions, the flow is considered steady. However, dynamic stall models are used to account for unsteady effects affecting the lifting lines sections.

1.2 Multibody systems modeling and analyses

Multibody systems (MBS) dynamics is the study of the motion of rigid bodies interconnected by joints that may undergo large translational and rotational displacements and are submitted to internal or external forces and torques. ROBOTRAN is symbolic software developed at UCL-MEED to model and analyse Multibody systems. The symbolic generation of multibody equations takes advantage of the manual and numerical techniques, allowing for drastic simplifications without any loss of generality compared to numerical generation. Multibody simulations with ROBOTRAN can be performed in a C, Matlab or Python environment; in this work only the C environment is used.

The symbolic translator of ROBOTRAN (MBSysTran) generates the MBS equations from the graphical description of the system given by the user in the graphical editor (MBSysPad). The equations are then automatically interfaced with the MBSysC program, and finally a 3D animation of the virtual system can be performed in the graphical editor (see Figure 1.3).

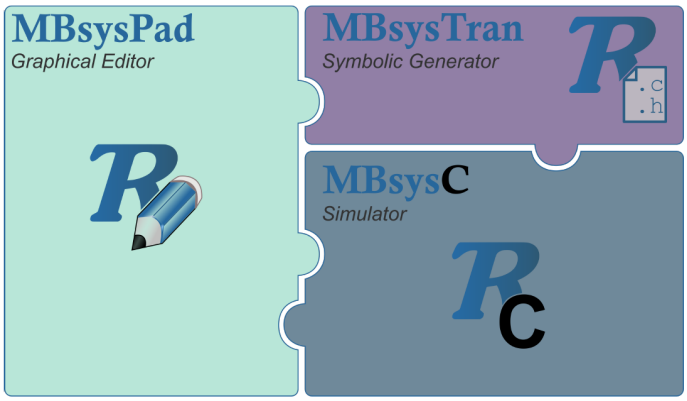

Figure 1.3: ROBOTRAN modules for C-code implementation [10].

In this section, the aspects of the multibody systems modeling and analyses necessary for the definition of the motion used by the flow solver will be described. First, some multibody conventions and notations used in ROBOTRAN are introduced. Next, the dynamic formalism for unconstrained MBS is presented, followed by a brief introduction to the symbolic generation. Finally, a special analysis feature useful in this work, the modal analysis, is detailed for the case of unconstrained MBS. For more exhaustive details about ROBOTRAN, the reader can refer to [10], [11] and [12].

1.2.1 Definitions and conventions

A multibody system is a mechanical system composed of N rigid bodies connected by joints. The structure of the system is either tree-like, when the number of rigid bodies is equal to the number of joints and there is only one path from one rigid body to any other, or a closed-loop

(Figure 1.4). In this work, only tree-like structures will be considered and the modeling of closed-loop structures will not be detailed.

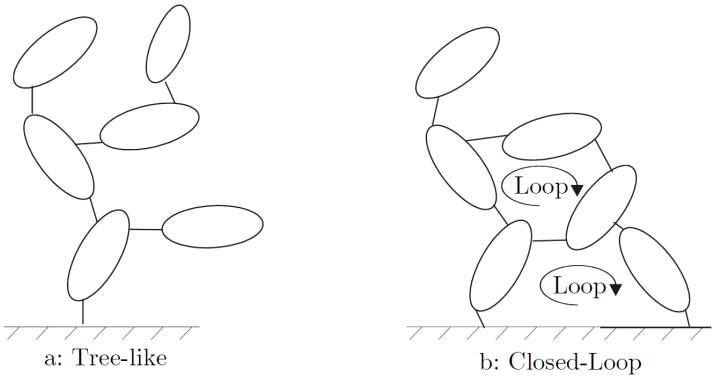

Figure 1.4: Tree-like versus closed-loop structures [11].

Bodies description

A body i must be carried by a parent body h through joint i and can have children bodies j and k. Each body i has an orthogonal right-handed body-frame $\{\hat{\mathbf{X}}^i\}$ rigidly attached to O^i, its reference attachment point of joint i. Denoting by $[\hat{\mathbf{I}}^i]$ and $[\hat{\mathbf{X}}^i]$ column matrices containing the reference vectors of the inertial frame $\{\hat{\mathbf{I}}\}$ and of the frame $\{\hat{\mathbf{X}}^i\}$, respectively, the body i is defined by (as represented in Figure 1.5) :

- $\mathbf{p}^i = [\hat{\mathbf{I}}]^T p^i$, the absolute position of point O^i,
- m^i and $\mathbf{I}^i = [\hat{\mathbf{X}}^i]^T I^i [\hat{\mathbf{X}}^i]$, the mass and the symmetric inertia tensor with respect to its center of mass G^i, respectively,
- $\mathbf{d}^{ii} = [\hat{\mathbf{X}}^i]^T d^{ii}$, the position vector of the center of mass G^i with respect to O^i,
- $\mathbf{d}^{ij} = [\hat{\mathbf{X}}^i]^T d^{ij}$, the position vector of the reference attachment point O'^j of the joint j, connecting a child j to the body i,
- $\mathbf{g} = [\hat{\mathbf{I}}]^T g$, the gravity vector.

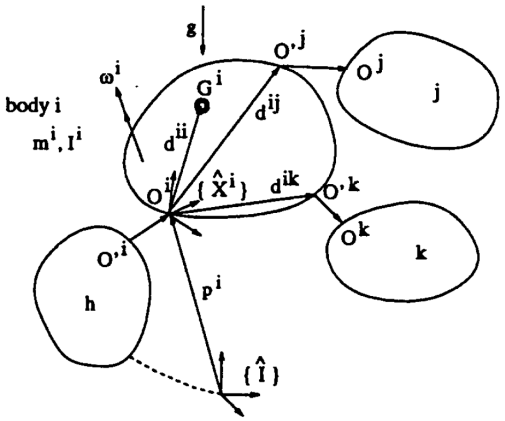

Figure 1.5: A body i in the multibody system [12].

Joints description

The joints are massless elements connecting two bodies at reference attachment points and allowing for relative motions. Every physical joint can be modeled in ROBOTRAN by a succession of two elementary types of single-degree-of-freedom joints, i.e., the prismatic and the revolute joints (Figure 1.6). At least one joint of the system is directly connected to an inertial body, called the base.

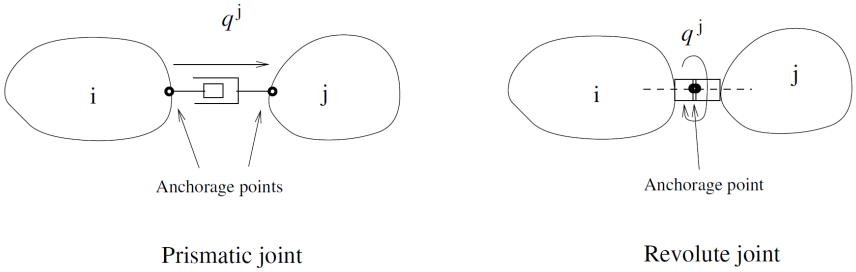

Figure 1.6: Elementary joints [10].

The relative displacement in the prismatic joint, or the rotation angle in the revolute joint, is represented by a generalized coordinate q^j associated with each joint j. A convention for the MBS modeling with ROBOTRAN considers a reference configuration of the tree-like system in which all the body-fixed frames $\{\hat{\mathbf{X}}^i\}$ coincide with the inertial frame $\{\hat{\mathbf{I}}\}$ and all the generalized coordinates are equal to zero ($q^i = 0$).

1.2.2 Dynamical equations

The equations describing the dynamics can be generated in the following semi-explicit form in terms of the generalized accelerations. The semi-explicit formulation is also referred to as the direct dynamics model in the literature.

Different multibody formalisms can be used to obtain the dynamical equations for tree-like structures MBS, such as the formalism based on the virtual power principle, the Newton-Euler recursive algorithm,etc. This equation expressed in terms of the generalized accelerations can be formulated in matrix form, also denoted as the semi-explicit form or direct dynamics model

$$M(q)\ddot{q} + c(\dot{q}, q, \delta, F_{ext}, L_{ext}, g) = \mathcal{Q} \tag{1.12}$$

where :

- M is the symmetric generalized mass matrix of the system,
- c is a nonlinear dynamic vector containing the Coriolis, centrifugal and gravity forces as well as the external forces F_{ext} and torques L_{ext},
- δ contains the dynamic parameters of the system (body masses, centers of mass) and the inertia matrices,
- $\mathcal{Q}$ represents the contribution of the joint force and torque.

Another more compact formulation of these equations, where the generalized accelerations are implicitly expressed, and referred to as inverse dynamics model, is given by

$$\Phi(\ddot{q}, \dot{q}, q, \delta, F_{ext}, L_{ext}, g) = \mathcal{Q}. \tag{1.13}$$

In ROBOTRAN, these equations are built from the graphical description of the system (MBSysPad) and several user functions describing the modeling features, such as the joint forces and torques, the external forces and torques, link forces and driven variables.

1.2.3 Symbolic generation

Instead of using a commercial symbolic generator, the ROBOTRAN generator was developed for two main reasons :

- for minimizing the amount of computer memory required for the generation of very large multibody models, making it possible on medium-sized computer without difficulties,
- for the possible simplifications of the symbolic expressions, more specifically for multibody equations.

The symbolic multibody equations consist of a set of C-code functions for calculating the various matrices and vectors of the equations of motion (Eq. 1.12). They are combinations of simple arithmetical operators $(+, -, *, /)$ and functions $(sin, cos, \sqrt{}, atan)$. Priority rules are formulated to consider a mathematical expression as a recursive tree whose leaves represent alphanumeric symbols. The terms and factors are then organized according to their nature, and trigonometric expressions are simplified according to elementary trigonometric formulae (e.g., the expression $a = 2cos(q^i)sin(q^i)$ is automatically replaced by $sin(2q^i)$). Finally, the set of equations is computed in a recursive manner, in which systematic recursive scalar variables and rules are used to minimize the computational cost.

1.2.4 Modal analysis

A modal analysis is the study of the dynamic properties of free systems in the frequency domain. The eigenmodes and eigenfrequencies of the system are calculated through this analysis and are useful for determining the stability and the resonance frequencies of the system.

Here, the modal analysis is performed from a linearization of the equation 1.12 around an equilibrium, denoted '*'. The numerical linearization provides the following system:

$$M_r(q^*)\Delta\ddot{q} + G_r(q^*, \dot{q}^*)\Delta\dot{q} + K_r(q^*)\Delta q = 0 \tag{1.14}$$

where $\Delta q = q - q^*$, M_r, G_r and K_r are the constant mass, damping and stiffness matrices respectively, found through the linearization procedure.

By defining x, such as

$$x = \begin{pmatrix} \Delta\dot{q} \\ \\ \Delta q \end{pmatrix} \rightarrow \dot{x} = \begin{pmatrix} \Delta\ddot{q} \\ \\ \Delta\dot{q} \end{pmatrix},$$

the system 1.14 can be written as

$$\begin{pmatrix} 0 & M_r \\ \\ M_r & G_r \end{pmatrix} \dot{x} + \begin{pmatrix} -M_r & 0 \\ \\ 0 & K_r \end{pmatrix} x = 0, \tag{1.15}$$

and finally in a first order form

$$\dot{x} = Ax \tag{1.16}$$

with

$$A = -\begin{pmatrix} 0 & M_r \\ \\ M_r & G_r \end{pmatrix}^{-1} \begin{pmatrix} -M_r & 0 \\ \\ 0 & K_r \end{pmatrix}. \tag{1.17}$$

By considering a particular solution $x(t)$ of 1.16 whose components have the same time dependency (harmonic, exponential), such as

$$x(t) = Ue^{\lambda t} \tag{1.18}$$

where U is the eigenvector and λ are the eigenvalues, the eigenvalue system is given by

$$(A - \lambda I)U = 0 \tag{1.19}$$

with I being the identity matrix.

1.3 Coupling of the flow and multibody solvers

The two previous sections describe the principal features of the flow solver and of the Multibody systems modeling tools. On one hand, the former predicts with precision the aerodynamic forces and the airflow behaviour when encountering lifting lines, but it is limited to manually written equations of motions of the lifting lines, making its application to high degrees of freedom cases difficult. On the other hand, ROBOTRAN generates efficient symbolic equations of the dynamic but cannot predict the aerodynamic forces applied on the bodies.

A coupling of both numerical tools was performed in order to combine the advantages of each of them. This section presents the coupling mechanism as described by [13].

1.3.1 Coupling strategy

In order to maintain the two previous codes untouched, a weak coupling was implemented. Unlike strong (or tight) coupling, the weak (or loose) coupling does not require the combination of to two tools into one system. Both run separately and are communicating information after a synchronization step. Due to the important computational cost of the flow solver, the latter is ruling the communication between both components.

The coupling operates as follows: at time t, the circulation is obtained by equation 1.10 and the aerodynamic forces are obtained by the airfoil aerodynamic coefficients. Those forces and the length of the time step are sent to ROBOTRAN that updates the dynamic data of the lifting lines over this time step. Subsequently, the lines data are sent back to the flow solver that sheds the vorticity in the flow as described in section 1.1.2.

1.3.2 Communication interface

In the flow solver, the kinematic is modeled by considering two types of bodies :

- "lifting lines" that contains the aerodynamic data and represent the slender blades or wings,
- "lifting bodies" to which the lifting lines are attached and that play a role in the dynamic computation. Taking the example of the modeling of an horizontal axis wind turbine, this body can be compared to the hub to which the blades are bolted.

The communication between both simulations relies on data structures containing the data specific to the Multibody system. These structures are organised in different levels and nested in each other. A global structure contains the structures of each Multibody system. In each system, a *mappingtable* structure contains the kinematic information of each lifting body (reference frame, position, velocity, accelerations,...) by means of "F-sensors". This *mappingbodies* structure finally contains all the lifting lines information in a *mappinglines* structure. This latter contains the kinematic information of the lines and the aerodynamic forces and torques. This topology is illustrated in figure 1.7.

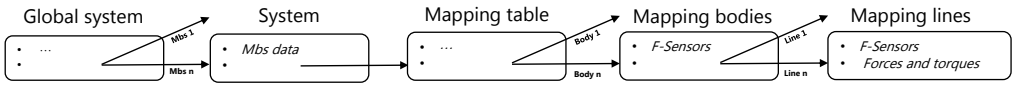

Figure 1.7: Illustration of the topology of the data structures.

The communication interface thus contains those structures as well as pre-processing, running and post-processing subroutines that allow the flow solver to lead ROBOTRAN. The running part is illustrated in figure 1.8.

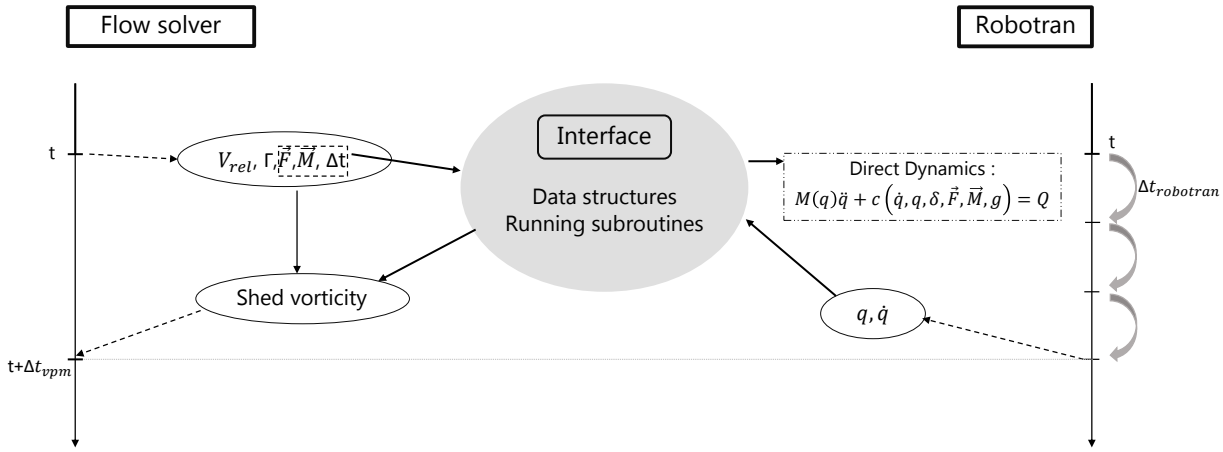

Figure 1.8: Illustration of the coupling strategy and communication interface.

Finally, let us note that in the pre-processing phase, the different bodies and "F-sensors" of ROBOTRAN are assigned to the corresponding lifting bodies and lines by a *mapping file* that also associates them to geometrical and aerodynamic data.

Chapter 2

Methodology

In the previous chapter, numerical tools for the modelling of complex dynamics in a flow solver were presented. However, each body was treated as a rigid unit, incapable of elastic deformation that real lifting surfaces frequently experience. As wings or blades behave in most of the cases as flexible bodies, their deformation can have implications in terms of performances and of stress generated.

Due to the enormous complexity that flexibility induces in terms of degrees of freedom, it would be impossible to take it into account manually in the flow solver. But the coupling of the flow solver with a multibody solver offers the possibility to treat the deformations in the latter.

Several methods exist to model the complex flexibility effects in multibody systems. Finite Element Methods (FEM) may be adopted to represent the components of the multibody system and consider elastic bodies. This approach is mainly focused on the flexibility effects and only uses the global multibody motion as a source of external and dynamical loading. Therefore, the computational cost is very high, and this method is not used in ROBOTRAN.

An assumed modes technique was proposed that considers an appropriate set of shape functions; it is based on the Timoshenko theory [11]. However, there is no systematic method for defining a set of shape functions depending on the problem. Moreover, at the time of writing, this method is not yet totally available in ROBOTRAN.

The "finite segment", or "lumped parameter" approach is more widely used to model Euler-Bernoulli beams in multibody systems modelling. Contrary to the Finite Element Methods, the flexibility effects are incorporated into the multibody dynamics analysis. This method is used here. It has the advantage to be simple in concept and to be applicable to a broad class of cases, and to give satisfactory and efficient results.

In this chapter, the finite segment approach and its integration into multibody systems is first detailed and then compared to simple testcases. Next, the inclusion of this method in the flow solver is presented.

2.1 The finite segment approach

The "finite segment" method, or "lumped-parameter" method, consists in replacing each flexible slender body of the system by a chain of N rigid bodies, or finite segments, connected by springs and dampers, as show in figure 2.1. The joints provide the degrees of freedom required for deformation to occur while the bodies, springs and dampers provide the inertial, restorative and dissipative forces that account for the deformation. Hence, it offers the advantage of dealing with flexible bodies in a pure rigid multibody context and it is straightforward with the existing coupling between the flow solver and ROBOTRAN. The method is intuitive and direct, resulting in a relatively simple formulation. It is also applicable to a large class of multibody systems. A disadvantage is the computational cost caused by increase in degrees of freedom. Indeed, for N segments, the number of degrees of freedom may be increased by 6N. However, next to the computational cost of the flow solver and thanks to the efficient symbolic generator of ROBOTRAN, this drawback is minor here.

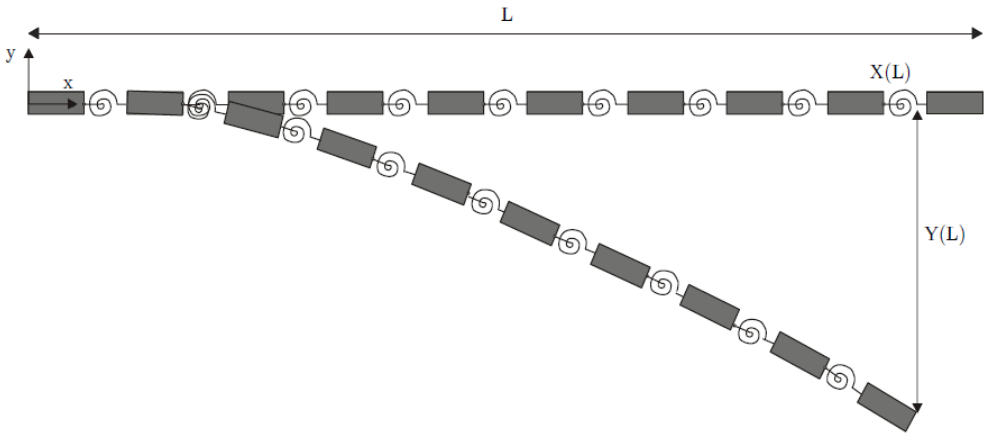

Figure 2.1: Illustration of the finite segment method [11].

Firstly, the procedure to identify the equivalent stiffness coefficients is described, as presented in [14] and [15]. Then, as a first validation step, results provided by this method for a uniform beam are compared to analytical solutions. A second validation step consists in comparing the results obtained for the modal analysis of a specific non-uniform wind turbine blade (NREL 5-MW) with the assumed modes approximation method.

2.1.1 Spring coefficients determination

Slightly different configurations exist for representing a beam element, as presented in [16]. They will be discussed later in this section. However, the procedure of the spring coefficients relies on the same principle and it is considered that the segments are small enough to capture the flexibility of the whole slender body.

The spring coefficients determination is based on the Euler-Bernoulli beam theory. This simple and widely used theory is based on the assumption that the cross-section of the beam is infinitely rigid in its own plane, i.e., no deformations occur in the plane of the cross-section [17].

According to Hooke's law, the torque τ_k exerted by a torsion spring is given by

$$\tau_k = k_R \theta, \tag{2.1}$$

where k_R is the rotational spring constant and θ is the angle of twist from its equilibrium position.

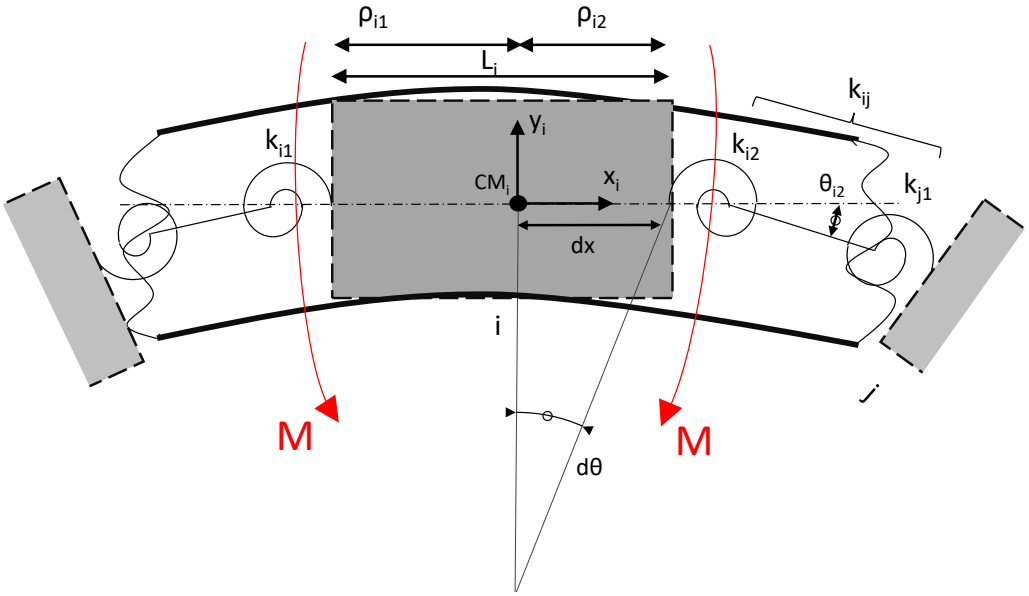

Figure 2.2: Illustration of an element in bending.

First, a beam segment subjected to bending is considered (figure 2.2). According to the Euler–Bernoulli beam theory, or classical beam theory, the relationship between the tip torque and rotational angle caused by deformation, for uniform elastic properties, is

$$M = E_i I_i \frac{\partial \theta}{\partial x}, \tag{2.2}$$

where M is the bending moment at the free end, E_i is Young's modulus of elasticity, I_i is the second moment of area ,and $\frac{\partial \theta}{\partial x}$ is the curvature. In the limit of small deflections, one can assume

$$\frac{\partial \theta}{\partial x} \simeq \frac{\theta_{i1}}{\rho_{i1}} \text{ and } \frac{\partial \theta}{\partial x} \simeq \frac{\theta_{i2}}{\rho_{i2}}, \tag{2.3}$$

with ρ_{i1} and ρ_{i2} being the distance between the center of mass of the segment CM_i and the extremities. The rotational spring coefficient of the springs at the extremities are thus given by

$$k_{i1} = \frac{E_i I_i}{\rho_{i1}} \text{ and } k_{i2} = \frac{E_i I_i}{\rho_{i2}}. \tag{2.4}$$

The equivalent spring modulus in bending joining two segments i and j must take into account the contribution of both segments. This corresponds to the placement of two springs, k_{i2} and k_{j1}, in series. The equivalent spring modulus k^b_{ij} for the spring segments in series is therefore given by

$$k^b_{ij} = \frac{k_{i2} k_{j1}}{k_{i2} + k_{j1}} = \frac{E_i E_j I_i I_j}{\rho_{j1} E_i I_i + \rho_{i2} E_j I_j}. \tag{2.5}$$

The same procedure can be applied to spring modulus in torsion k^t_{ij}, giving

$$k^t_{ij} = \frac{G_i G_j J_i J_j}{\rho_{j1} G_i J_i + \rho_{i2} G_j J_j} \tag{2.6}$$

with G the shear modulus and J the torsion constant.

2.1.2 Validation 1 : uniform cantilever beam

In [14], some examples are presented to illustrate the validity of the method. Here, a study of the effect of the number and configuration of segments will be carried out with a uniform cantilever beam, which allows for an analytical solution provided by the classical beam theory.

Let us consider a cantilever beam with uniform structural and geometrical properties. In this particular case, and taking N identical segments of length $l = L_{tot}/N$, then

$$k_{ij}^b = \frac{EI}{l} \text{ and } k_{ij}^t = \frac{GJ}{l}. \tag{2.7}$$

It was observed that two different conceptual configurations are possible, depending on how each beam element is considered, and mostly on the extremities of the beam, as shown in figure 2.3.

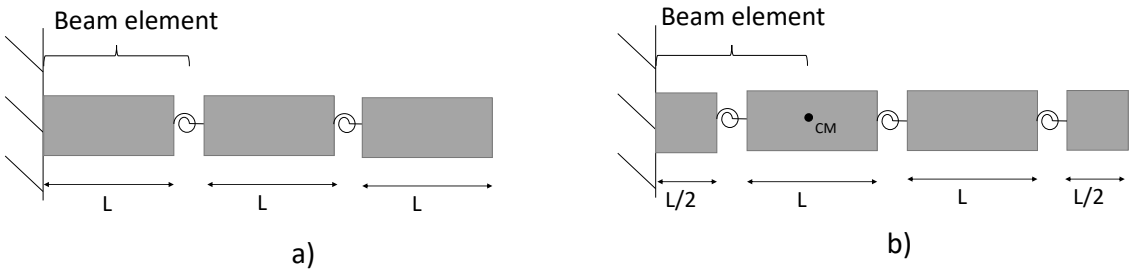

Figure 2.3: Two different configurations for the extremities.

(a) In the first configuration, see figure 2.3.a), the segments of the extremities have the same length as the other segments. The flexibility aspect of the element is thus transferred to the extremity of each element. This configuration is sometimes referred to as Duncan's model.

(b) The second configuration is actually composed of N+1 rigid segments and N beam elements, see figure 2.3.b), but the length of the non-extremity segments is equal as in the previous case, and the equivalent spring constants follow the expression of equation 2.5. The flexibility aspect of the element is thus transferred to the center of the element. This configuration can be referred to as Rayleigh's model.

Length, L	Width, W	Thickness, T	Density, ρ
0.3 m	0.015 m	0.005 m	2800 kg/m^3
Young's Modulus, E	Shear Modulus, G	Second moment of area, I_z	Torsion Constant, J
70e9 Pa	2.6e10 Pa	1.563e-10 m^4	4.9313e-10 m^4

Table 2.1: Uniform aluminium beam properties

The properties of the aluminium beam used are summarized in table 2.1, based on the case described in [18].

Modal analysis

Considering the theory of Euler-Bernoulli applicable to this beam subjected to small deformations, the natural frequencies in bending are obtained by solving

$$cos\Big(\sqrt{\frac{\omega}{a}}L\Big)cosh\Big(\sqrt{\frac{\omega}{a}}L\Big) = -1, \tag{2.8}$$

where $a^2 = EI/\rho A$ with , as detailed in appendix A.

The frequencies obtained by equation 2.8 are compared with those obtained by performing a modal analysis in ROBOTRAN (as detailed in section 1.2.4) for a finite segment method with 5, 10, 15 and 20 beam elements. The results obtained with Duncan's model (case (a)) and Rayleigh's model (case (b)) are summarized in table 2.2 and 2.3, respectively.

Mode	**Analytical**	**N = 5**		**N = 10**		**N = 15**		**N = 20**	
	Freq (Hz)	Freq (Hz)	Err (%)	Freq (Hz)	Err (%)	Freq (Hz)	Err (%)	Freq (Hz)	Err (%)
1	44.87	48.6	8.3	45.84	2.2	45.31	1.0	45.12	0.6
2	281.21	334.7	19.0	298.7	6.2	289.2	2.8	286.0	1.7
3	787.39	907.5	15.3	851.7	8.2	820.7	4.2	807.2	2.5
4	1543	1702	10.3	1673	8.4	1621	5.1	1591	3.1

Table 2.2: Comparison of the natural frequencies in bending of a uniform cantilever beam between (i) the analytical solution and (ii) the modal analysis performed on the finite segment model in configuration (a).

Mode	**Analytical**	**N = 5**		**N = 10**		**N = 15**		**N = 20**	
	Freq (Hz)	Freq (Hz)	Err (%)	Freq (Hz)	Err (%)	Freq (Hz)	Err (%)	Freq (Hz)	Err (%)
1	44.87	45.28	0.9	44.92	0.1	44.92	0.1	44.90	0.1
2	281.21	290.3	3.2	283.4	0.8	282.1	0.3	281.7	0.2
3	787.39	796.9	1.2	796.9	1.2	791.2	0.5	789.2	0.2
4	1543.0	1567	1.5	1567	1.6	1553	0.6	1547	0.3

Table 2.3: Comparison of the natural frequencies in bending of a uniform cantilever beam between (i) the analytical solution and (ii) the modal analysis performed on the finite segment model in configuration (b).

The analysis of the results demonstrate the efficiency of the method for a sufficient number of segments. According to [16], for large number of beam elements N, the error decreases according to $\mathcal{O}(1/N)$. This tendency is observed in the results (error decreasing in $1/2N$ approximately). It can be seen that the numerical solution slightly overestimates the frequency. Besides, the precision is always lower for higher modes. This comes from the fact that the short oscillations of higher modes are less well captured by the finite segments (see figure 2.4). Finally, it is observed that the Rayleigh configuration (case (b)) at the extremities of the beam provides a better capture of the modes in bending of this beam than does the Duncan configuration (case (a)).

Deflection

Let us now study the tip deflection of the beam subjected to a uniform load. From the Euler-Bernoulli theory, the tip deflection of a cantilever beam subjected to a uniform gravitational

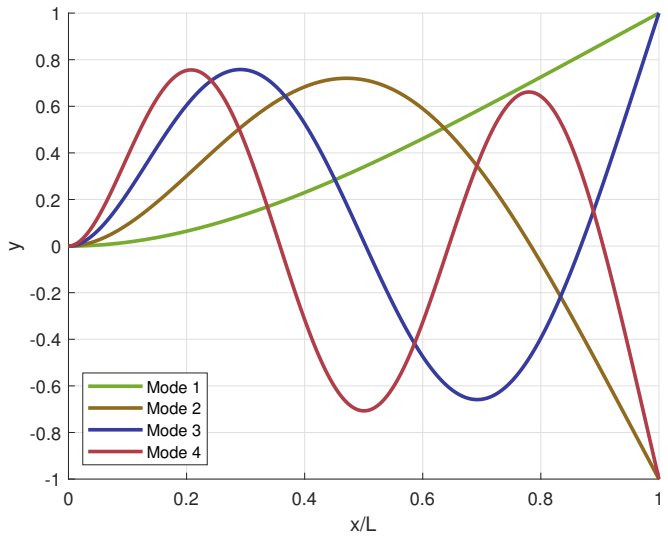

Figure 2.4: Mode shapes of the first four modes of vibration of a uniform cantilever beam in bending.

load is

$$\delta = \frac{mg}{L}\frac{L^4}{8EI}. \tag{2.9}$$

The results obtained in the two configurations previously presented are compared to the results of the analytical solution in table 2.4.

Analytical		**N = 5**		**N = 10**		**N = 15**		**N = 20**	
δ (m)		δ (m)	Err (%)	δ (m)	Err (%)	δ (m)	Err (%)	δ (m)	Err (%)
1.907e-4	a	1.617e-4	15.2	1.823e-4	4.4	1.868e-4	2.0	1.884e-4	1.2
	b	1.869e-4	2.0	1.898e-4	0.5	1.903e-4	0.2	1.905e-4	0.1

Table 2.4: Comparison of the tip deflection of a uniform cantilever beam between (i) the analytical solution and (ii) the analysis performed on the finite segment model in the configurations (a) and (b).

In addition to the fact that, as previously mentioned, the increase in the number of beam elements provides results whose error decreases in $\mathcal{O}(1/N)$, it appears more clearly that the Rayleigh configuration (case (b)) is far more precise than the Duncan configuration (case (a)) for a cantilever beam. The results obtained for Rayleigh's model are very satisfying and prove the consistency of the finite segment method for a sufficient number of segments.

Torsion

Finally, let us analyse the free vibration in torsion. As seen in the previous section, the Rayleigh configuration provides results of a far higher precision than with the Duncan configuration. Therefore, the latter will not be used anymore in the rest of the work. The comparison between the numerical solution and the solution provided by the beam theory

$$cos\Big(\frac{\omega}{a}x\Big) = 0, \tag{2.10}$$

with $a^2 = GJ/I_0$ (see appendix A), is provided in table 2.5.

Once again, satisfactory results are obtained for a sufficient number of segments. The first mode is captured with great precision for small amounts of segments, but for higher modes it is necessary to use more segments for capturing the torsional mode shapes (see figure 2.5).

Mode	Analytical	N = 5		N = 10		N = 15		N = 20	
	Freq (Hz)	Freq (Hz)	Err (%)	Freq (Hz)	Err (%)	Freq (Hz)	Err (%)	Freq (Hz)	Err (%)
1	1427	1421	0.4	1425	0.1	1425	0.1	1426	0.1
2	4280	4123	3.7	4240	0.9	4248	0.7	4267	0.3
3	7133	6422	10	6951	2.6	6988	2.0	7072	0.9

Table 2.5: Comparison of the natural frequencies in torsion of a uniform cantilever beam between (i) the analytical solution and (ii) the modal analysis performed on the finite segment model in configuration b.

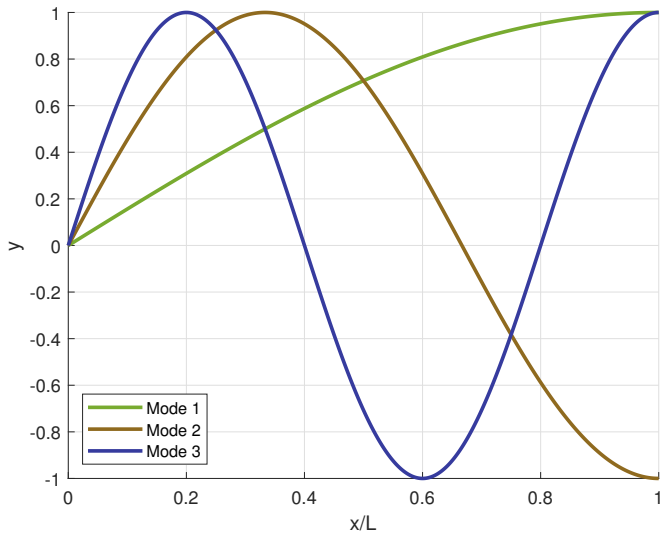

Figure 2.5: Mode shapes of the first three vibration modes of a uniform cantilever beam in torsion.

2.1.3 Validation 2 : NREL 5-MW wind turbine blade

Now, let us apply the finite segment method to a non-uniform case that is also a lifting surface. A consistent benchmark is given by the NREL 5-MW reference turbine, whose structural and aerodynamic properties are defined in [19].

A modal analysis is performed to determine the consistency of the finite-segment method in the case of a non-uniform beam. Flap-wise, edge-wise and torsional natural modes (see figure 2.6) are analysed and compared to a numerical assumed mode method.

As the mass distribution and elastic stiffness of the blade are complicated functions it is not possible to arrive at a simple analytical solution of the blade bending equation [21]. The numerical approximated results are obtained by using the assumed modes method, as presented in appendix B, considering no rotation ($\Omega = 0$).

The results for the free vibration in flap-wise bending, edge-wise bending and in torsion are compared to the numerical results in table 2.6, 2.7 and 2.8, respectively. The results obtained with the assumed modes method are obtained for $n = 8$ in equation B.1.

The overall trend is broadly similar to that observed is the previous section. Indeed, the precision globally increases with the number of segments used, mostly at higher modes.

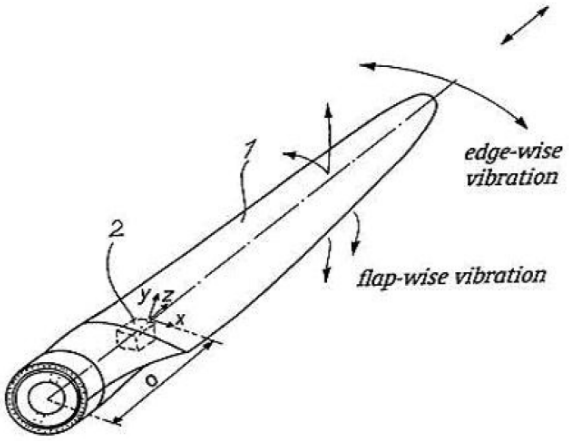

Figure 2.6: Edge-wise and flap-wise vibrations of the blade [20].

Mode	**Assumed modes**	**N = 5**		**N = 8**		**N = 10**		**N = 15**	
	Freq (Hz)	Freq (Hz)	Err (%)	Freq (Hz)	Err (%)	Freq (Hz)	Err (%)	Freq (Hz)	Err (%)
1	0.678	0.697	2.7	0.699	3.1	0.697	2.7	0.696	2.7
2	1.921	1.977	2.9	1.994	3.8	1.990	3.6	1.980	3.1
3	4.412	4.523	2.5	4.564	3.4	4.556	3.3	4.542	2.9
4	7.800	6.300	19.2	7.958	2.0	8.076	3.5	8.081	3.6

Table 2.6: Comparison of the natural frequencies in flap-wise bending of a NREL-5MW blade for 5, 8, 10 and 15 finite beam elements.

Mode	**Assumed modes**	**N = 5**		**N = 8**		**N = 10**		**N = 15**	
	Freq (Hz)	Freq (Hz)	Err (%)	Freq (Hz)	Err (%)	Freq (Hz)	Err (%)	Freq (Hz)	Err (%)
1	1.059	1.101	4.0	1.110	4.8	1.102	4.0	1.098	3.5
2	3.857	4.072	5.6	4.104	6.4	4.073	5.6	4.043	4.8
3	8.798	9.472	7.7	9.389	6.7	9.426	7.1	9.302	5.7
4	15.967	16.85	5.5	16.92	6.0	17.11	7.2	16.91	5.9

Table 2.7: Comparison of the natural frequencies in edge-wise bending of a NREL-5MW blade for 5, 8, 10 and 15 finite beam elements.

Mode	**Assumed modes**	**N = 5**		**N = 8**		**N = 10**		**N = 15**	
	Freq (Hz)	Freq (Hz)	Err (%)	Freq (Hz)	Err (%)	Freq (Hz)	Err (%)	Freq (Hz)	Err (%)
1	5.565	5.512	1.0	5.543	0.4	5.572	0.1	5.575	0.2
2	9.706	9.152	5.7	9.494	2.2	9.611	1.0	9.687	0.2
3	14.614	11.92	18.4	13.63	6.7	13.94	4.6	14.40	1.5
4	19.796	13.94	29.6	17.26	12.8	18.19	8.1	19.04	3.8

Table 2.8: Comparison of the natural frequencies in torsion of a NREL-5MW blade for 5, 8, 10 and 15 finite beam elements.

In bending, the solution obtained with the finite segment approach provides a higher natural frequency than with the assumed modes method. Indeed, the latter is an approximation method. The results depend on the number n of combined approximation functions. As the superposition of 8 approximate functions is considered here, a better fit of the higher modes is provided. The relatively important differences between both methods for the first mode, compared to the results obtained in the previous section, do not necessarily mean a worse capture of the flexibility effects for non-uniform bodies by the finite segment methods.

A finite element modelling of the NREL 5-MW blade vibrations is performed by [22]. The results are provided in table 2.9. It can be seen that the results obtained with the finite segment method in ROBOTRAN show good agreement with these latter results.

Mode	Natural frequency [Hz]	
	flap-wise	edge-wise
1	0.692	1.109
2	1.998	4.080
3	4.655	9.441
4	8.249	-

Table 2.9: Natural frequencies of the NREL 5-MW blade obtained by finite element modelling [22].

Remark about damping

No damping coefficient model is proposed for the finite segment method. In most flexible multibody dynamics formulations, the use of structural damping is not considered [15]. Based on the proposition made in [18], a simple linear rule with the spring coefficient will be used.

Considering an ideal viscous dashpot for modelling the dissipation, the damping torque τ_c is proportional to the instantaneous angular velocity

$$\tau_c = c_R \dot{\theta}, \tag{2.11}$$

where c_R is the rotational damping coefficient and θ is the angular position. It has been observed, by the use of the modal analysis tool provided by ROBOTRAN (described in section 1.2.4), that for a damping coefficient proportional to the spring coefficient, the damping ratio itself is proportional to the damping coefficient, and therefore also to the spring coefficient:

$$\zeta = \alpha c_R = \beta k_R, \tag{2.12}$$

where ζ is the damping ratio, α and β are "empirical" proportionality constants and k_R is the rotational spring constant.

In the case where the structural damping ratio is provided, the damping coefficient can easily be empirically determined, based on the spring coefficients. This is the case for the NREL 5-MW wind turbine blade benchmark. The structural damping ratio is set at 0.477465% for all modes [19]. Actually, the damping coefficient is of course proper to each eigenmode. Depending on which mode is the most excited, the calibration can be done to match the coefficient ratio of the principally excited mode.

As an example, let us consider this wind turbine blade in flap-wise bending. When the first mode is predicted to be the most excited, the proportionality constant β/α, such that for each joint i the damping coefficient is given by

$$c_R^i = \frac{\beta}{\alpha} k_R^i, \tag{2.13}$$

is $\beta/\alpha = 0.0022$, independently of the number of segments used.

2.1.4 Conclusion

The previous examples demonstrated the efficacy of the finite segment method for modelling uniform and non-uniform flexible cantilever beams. Plenty of other quantitative examples exist, see for instance [11], [14].

The finite segment can therefore be used to model the flexibility effects of lifting surfaces in bending and in torsion. However, care must be taken to select sufficient number of segments in order to capture adequately the principal vibration modes.

However, the design of the system must be done manually and requires a heavier workload for a higher number of segments. Indeed, in addition to the spring coefficients, the geometrical, mass and inertial properties of each segment must be provided to MBsysPad, the graphical editor of ROBOTRAN (see figure 1.3). Moreover, increasing the number of segments causes an increases in the number degrees of freedom, and hence in the computational cost.

A trade-off has to be found between the precision of the motion capture and the implementation and computational workload. It can be concluded that a minimum of 10 finite segments is required, and that over 20 segments, the implementation cost becomes too high for the user (see figure 2.7) and only minor benefits are obtained.

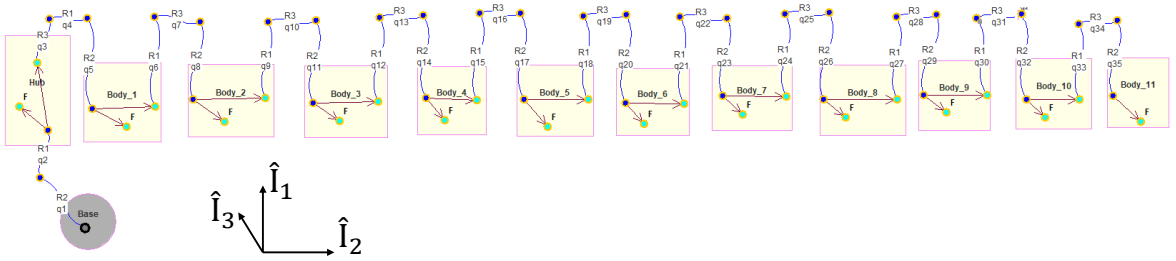

Figure 2.7: MBsysPad model of the NREL 5-MW blade discretized in 10 segments according to Rayleigh's model

It was also shown that, for cantilever beams, Rayleigh's model provides better results than the Duncan configuration. The latter will therefore not be used.

Finally, the damping factor must be found empirically to match the benchmark by determining a proportionality constant between the spring coefficients and the damping coefficients.

The finite segment approach thus provides precise results, dealing with the flexibility effects in a conceptually simple way by using pure rigid bodies. The drawback of the method is that its implementation is problem-dependent, and requires some intuition or analysis by the analyst to determine the correct parameters.

remark In the present section, the number N was assigned to the number of beam elements, as defined in figure 2.3. In the following sections, the number of elements, or segments, will refer to the number of rigid bodies used to discretize the beam.

2.2 Integrating the finite segment approach in the flow solver

In the previous section, the handling of the flexibility effects in a multibody system solver was described. Thanks to the coupling between ROBOTRAN and the flow solver, the integration of the finite segment method for modelling flexible lifting lines is almost direct. However, some features were added for two reasons:

- In the pre-processing phase of the coupling procedure, the definition of the lifting lines via a *mapping file* must be adapted to the case of lines discretized into multiple elements.
- Due to this discretization into rigid lines, the junctions between the lines generate unrealistic angles that cause vorticity shedding (see figure 2.8). To avoid this problem, interpolations are performed to obtain curved lifting lines.

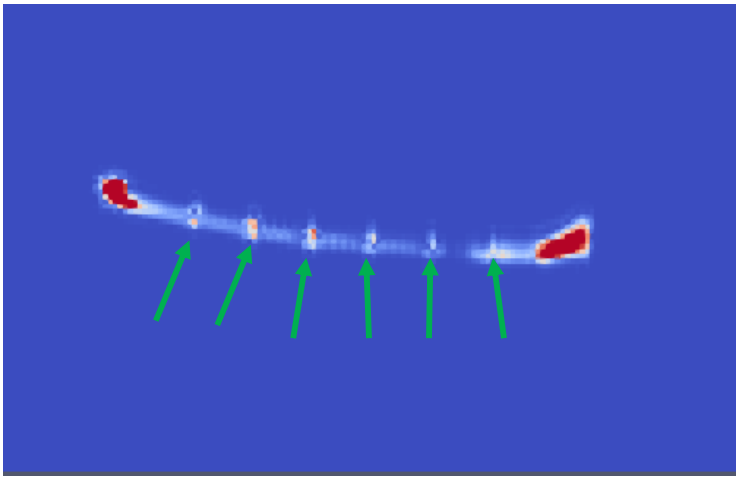

Figure 2.8: Illustration of the parasitic vorticity generated at the intersection of the segments for a blade discretized in 8 elements.

2.2.1 Modifications in the treatment of the mapping file

As explained in section 1.3, in the pre-processing phase, the bodies and sensors defined in ROBOTRAN are associated to lifting bodies and lines used in the flow solver. The connection is made by a *mapping file* containing the indices of each body, line and sensor as well as a geometrical file and a polar data file associated to each line.

The line geometrical file contains the distributed airfoil geometrical properties, such as the aerodynamic center position, the chord length and orientation, etc. The line polar data file provides aerodynamic information about the lifting line at defined Reynolds numbers. These files defining a whole rigid lifting line, as well as the *mapping file*, must be provided by the user, and are treated in the coupling interface in order to be correctly read by the flow solver.

Modifications are introduced so that the mapping file format remains unchanged and can be used for both rigid and flexible lifting lines. The only difference for the user is that for flexible lifting lines, all the indices of the finite segments must be specified. Based on the MBS file, the geometry and polar files are then reshaped and the new files are attributed to each

segment. The reshape relies on linear interpolations between the airfoil sections. Figure 2.9 illustrates the handling of the finite segments definition by the mapping file and the coupling interface.

These modifications offer an accessible flexible model implementation and allow for fast geometrical modifications of the MBS model without any changes in the lifting lines data. They have been tested in multiple configurations, however the format of the *mapping file* must be strictly respected.

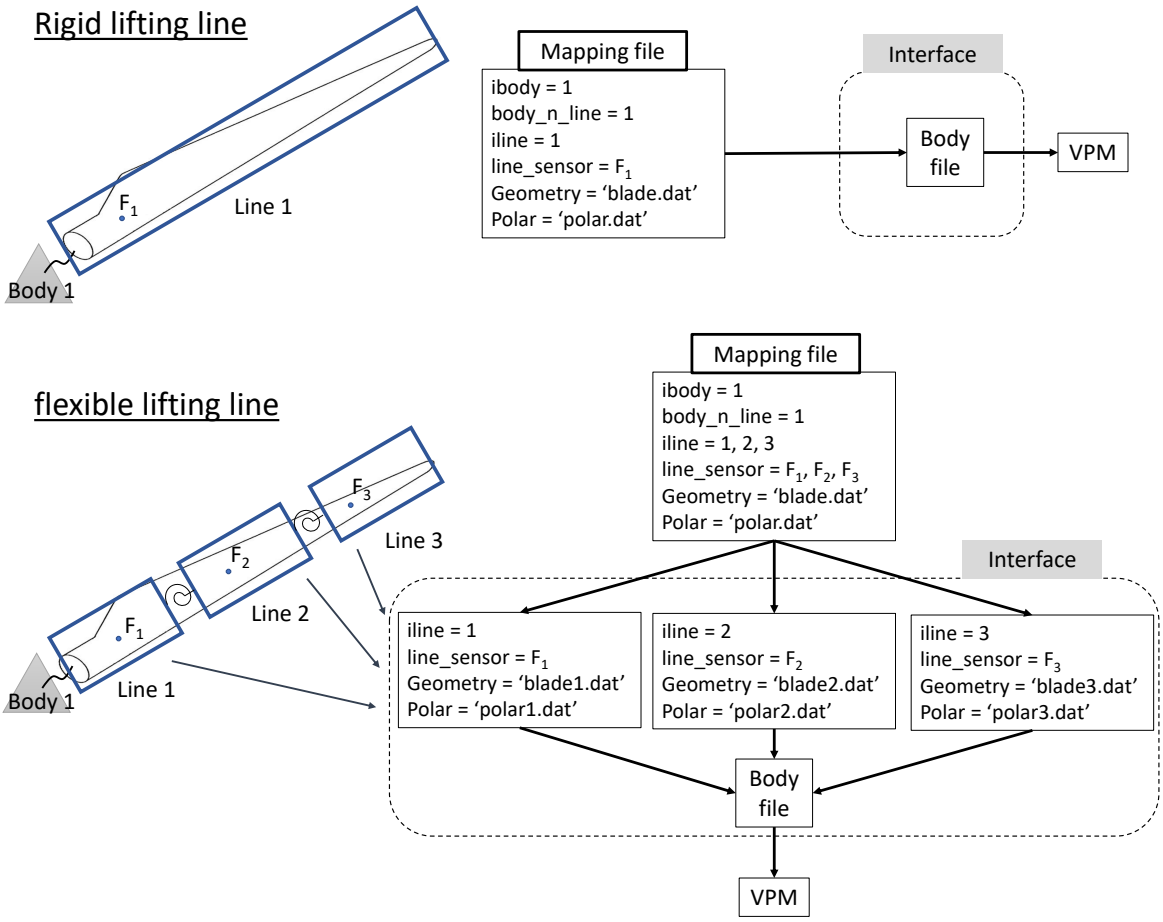

Figure 2.9: Handling of the finite segments by the coupling interface

2.2.2 From rigid segments to a curved line

Even if the number of finite segments chosen is large, irregularities appear at the positions of the joints. To deal with this problem and come closer to more realistic curved flexible lines, interpolations are performed. Indeed, as mentioned earlier, there is no affordable exact analytical solution for deformed non-uniform bodies.

Position interpolation

The interpolation is based on the combination of shape functions, interpolating the positions between defined discrete points of the lifting line. The shape functions chosen are derived from the first vibration mode shapes of a uniform cantilever beam, i.e., of uniform structural and geometrical properties (see appendix A). Actually, these functions do not exactly correspond with the mode shapes of a non-uniform beam (see figure 2.10). However, since we are in the

hypothesis of small deformations, as in the Euler-Bernoulli beam theory and with the finite segment method, these functions may constitute appropriate shape functions applicable to a wide range of cases. Moreover, the closer the slender wing gets to a uniform slender body, the more accurate the interpolation (e.g., helicopter blades, rectangular wings, etc).

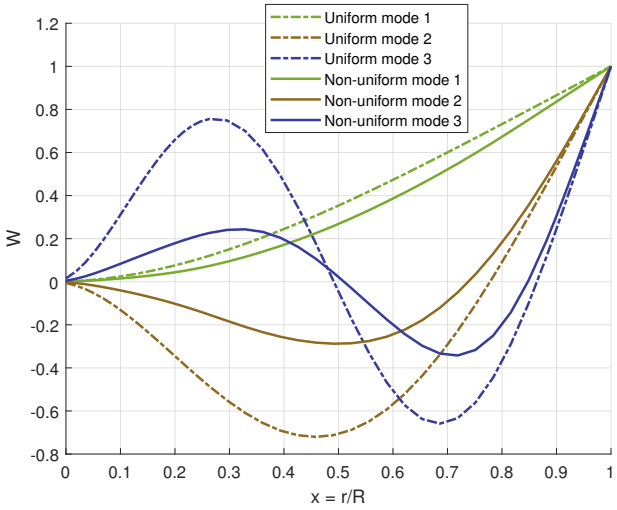

Figure 2.10: Mode shapes of the first three vibration modes of a uniform cantilever beam and of a NREL 5-MW wind turbine blade in bending.

In practice, for a number n of finite segments for one lifting line, n control points are chosen on the line. As the Rayleigh configuration is chosen for cantilever bodies, the control points are defined as follows:

- on the extremity segments, the control points are the extremities themselves (clamped end and free end),
- on the other segments, the control points are at the geometric center of the segment,

as illustrated in figure 2.11.

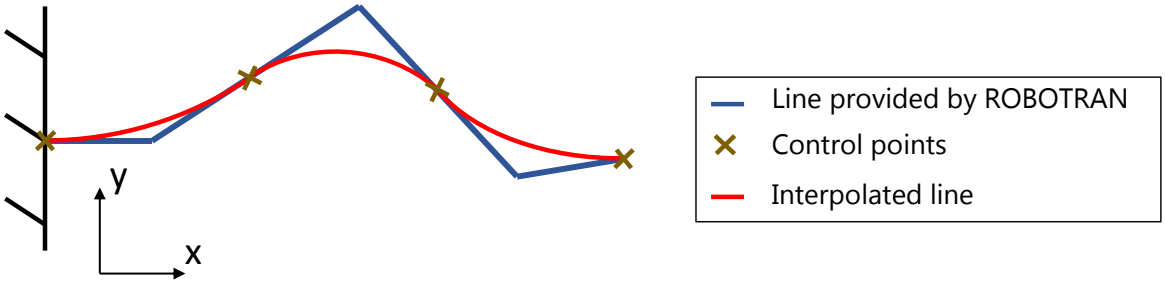

Figure 2.11: Illustration of the interpolation of the line in deflection.

Considering bending with deflections in the y direction, the deflection at a control point i can be expressed as a set of shape functions

$$y_i = \sum_{j=1}^{n} a_j f_j(x_i) \tag{2.14}$$

where a_j is a coefficient to be determined and $f_j(x_i)$ is the value of the j^{th} shape function at the position x_i.

The contribution of the high order functions, corresponding to high modes, may lead to bad results. Therefore, for n control points, the $n/2$ first shape functions, for the case of bending, are given by

$$f_j(x) = \frac{1}{2}\left[\left(\frac{sin\left(\beta_j\right) - sinh\left(\beta_j\right)}{cosh\left(\beta_j\right) + cos\left(\beta_j\right)}\right)\left(sinh\left(\beta_j\frac{x}{L}\right) - sin\left(\beta_j\frac{x}{L}\right)\right) + \left(cosh\left(\beta_j\frac{x}{L}\right) - cos\left(\beta_j\frac{x}{L}\right)\right)\right], \quad (2.15)$$

where β_j are the roots of the equation $cosh(\beta_j)cos(\beta_j) = 1$ and L is the total length of the beam (see appendix A). The last $n/2$ shape functions are given by

$$f_j(x) = \frac{1}{2}\left[\left(\frac{sin\left(\beta_{j-n/2}\right) - sinh\left(\beta_{j-n/2}\right)}{cosh\left(\beta_{j-n/2}\right) + cos\left(\beta_{j-n/2}\right)}\right)\left(sinh\left(\beta_{j-n/2}(1-\frac{x}{L})\right) - sin\left(\beta_{j-n/2}(1-\frac{x}{L})\right)\right) + \left(cosh\left(\beta_{j-n/2}(1-\frac{x}{L})\right) - cos\left(\beta_{j-n/2}(1-\frac{x}{L})\right)\right)\right] \quad (2.16)$$

where $\beta_{j-n/2}$ corresponds to the first $n/2$ roots of the equation $cosh(\beta_j)cos(\beta_j) = 1$.

This technique requires the number of control points, and therefore of segments, to be even. It is compatible with a wide number of configurations. The shape functions for $n = 4$ are presented in figure 2.12.

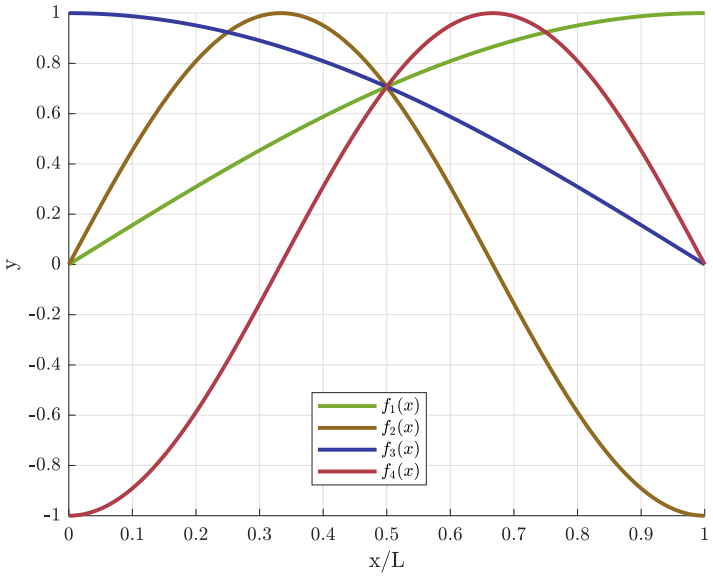

Figure 2.12: Illustration of the shape functions for 4 control points.

Finally, solving the system of equations 2.14 provides the coefficients a_j, and the interpolated positions of the line are obtained by

$$y = \sum_{j=1}^{n} a_j f_j(x). \quad (2.17)$$

The same reasoning can be applied to torsion angle θ, with the shape functions given by

$$f_j(x) = sin\Big(\beta_j \frac{x}{L}\Big), \tag{2.18}$$

where β_j are the roots of $cos(\beta_j) = 0$.

Relative velocity and orientation adaptations

As explained in section 1.1.2, in the flow solver, the lifting lines are discretized into blade elements with a spacing approximately corresponding to the mesh spacing. On these blade elements, probes contain all the geometrical and aerodynamic information (position, velocity, orientation, angle of attack, lift, etc). The interpolation described previously only modifies the position of the probes. However, the velocity and orientations must also be modified, to correspond to their new position.

As a reminder, since we are in the hypothesis of small deformations and with a sufficient number of finite segments to capture the flexibility effects, the velocity and orientation of the interpolated line relative to those of the line provided by ROBOTRAN are of small scale. These values are therefore obtained from first order finite differences. The new orientations are obtained from the adjacent probes (central differences), and the relative velocity is obtained from the relative position at the current and at the previous time steps (backward differences).

All these interpolations are performed at each time step, directly on the data provided by ROBOTRAN to the flow solver.

Chapter 3

Results

The handling of the flexibility effects in the flow solver was presented in the previous chapter. This chapter covers the application of the new features to different configurations. The first two applications are used to validate the model, by comparing the results with analytical solutions that are presented. Finally, the full NREL-5MW blade in rotation will be studied, and a comparison of the aerodynamic torque between the rigid and flexible case will be performed.

3.1 Validation 1 : Uniform rectangular wing

In order to demonstrate the validity of the features added to capture flexibility effects, some validations steps are performed. The first consists in the vertical deflection of half of a uniform rectangular wing. This configuration allows the comparison with an exact analytical solution based on the lifting line theory and on the classical beam theory.

3.1.1 Testing configuration

An illustration of the MBS model is given in figure 3.1. The rectangular wing is half rigid and half flexible. The flexible part can thus be seen as a cantilever beam.

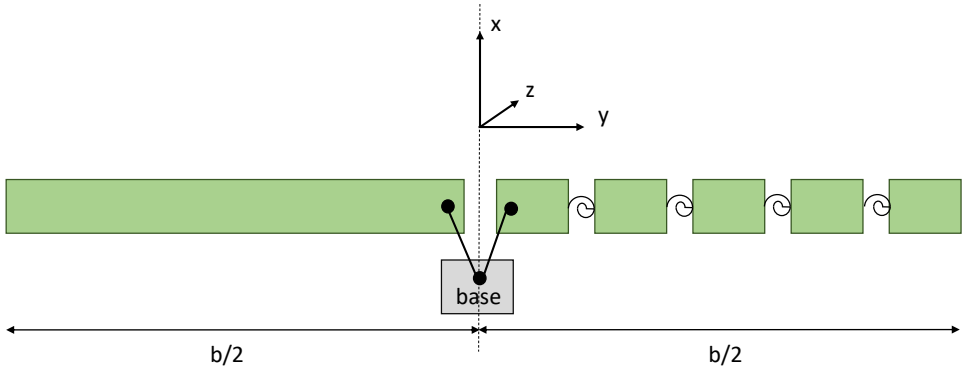

Figure 3.1: Illustration of the MBS model of the rectangular wing.

No movement is allowed other than rotations about the z axis between the finite segments. In order to adequately capture the flexibility effects and to respect the constraint of an even number of rigid segments, the flexible half of the wing is discretized into 12 segments.

The wing has the following properties :

- the aspect ratio is $AR = 20$,

- the wing is not twisted and the geometric angle of attack is $\alpha_g = 5[^\circ]$,
- the aerodynamic profile is considered to follow the thin airfoil theory and the slope of the lift curve $C_{l,\alpha}$ is equal to 2π,
- the wing is made out of aluminium, and its Young modulus is $E = 70GPa$
- on its cross section, the profile is assumed to be an ellipse of minor axis 10 times smaller than the major axis.

The wing is submitted to a uniform flow pointing toward the z direction. The Reynolds number with respect to the chord c is $Re_c = \frac{\rho U_\infty c}{\mu} = 1.274 \cdot 10^6$ and no gravity effects are considered.

3.1.2 Analytical solution

The deflection of the wing can be obtained by combining the lifting line theory to obtain the vertical load with the Euler-Bernoulli beam theory, or classical beam theory, to determine the deflection.

According to the Kutta-Joukowsky theorem, the lift and induced drag per unit length of the airfoil are given by

$$l(y) = \rho U_\infty \Gamma(y) \text{ and } d_i(y) = \epsilon(y)\rho U_\infty \Gamma(y) \tag{3.1}$$

where ρ, U_∞ and Γ are the fluid density, the fluid velocity and the local circulation, respectively. ϵ is the effective velocity vector as seen by the profile, or induced downwash angle. Operating the change of variable for the spanwise coordinates y,

$$y(\theta) = -\frac{b}{2} sin(\theta) \text{ with } 0 \ \leq \theta \leq \pi \tag{3.2}$$

with b being the span length, the local circulation and induced downwash angle can be modelled using the following Fourier series approximation

$$\Gamma(y) = \Gamma(\theta) = U_\infty b \sum_{n=1,3,\ldots}^{\infty} B_n sin(n\theta), \tag{3.3}$$

and

$$\epsilon(\theta) = \frac{1}{2} \sum_{n=1,3,\ldots}^{\infty} n B_n \frac{sin(n\theta)}{sin(\theta)}. \tag{3.4}$$

Due to the symmetry of the wing, the coefficients B_n are zeros for n being even. These coefficients are determined by the following compatibility equation

$$\sum_{n=1,3,\ldots}^{\infty} B_n sin(n\theta) = \frac{1}{2} a_0(\theta) \frac{c(\theta)}{b} \Big[\alpha_g(\theta) - \frac{1}{2} \sum_{n=1,3,\ldots}^{\infty} n B_n \frac{sin(n\theta)}{sin(\theta)}\Big], \tag{3.5}$$

where a_0, c and α_g are constant and $a_0 = 2\pi$ in this case.

With the lift and drag distribution, the bending moment distribution on the flexible half of the wing is obtained by

$$M(y) = \int_y^{b/2} (cos(\alpha) l(y) + sin(\alpha) d(y)) y dy. \tag{3.6}$$

According to the Euler-Bernoulli beam theory, the equation describing the deflection w of a uniform beam is

$$\frac{\partial^2 w}{\partial y^2} = \frac{M(y)}{E I_z}, \tag{3.7}$$

that can be integrated to obtain the displacement distribution, paying attention to compliance with the geometrical boundary conditions.

3.1.3 Results

The deflection distribution of the flexible half of the wing in steady-state, i.e., after stabilisation, obtained on one hand with analytical results and on the oder hand with the flow solver and the finite segment method is presented in figure 3.2. The numerical results are presented for two different configurations of probes on the flexible lifting line.

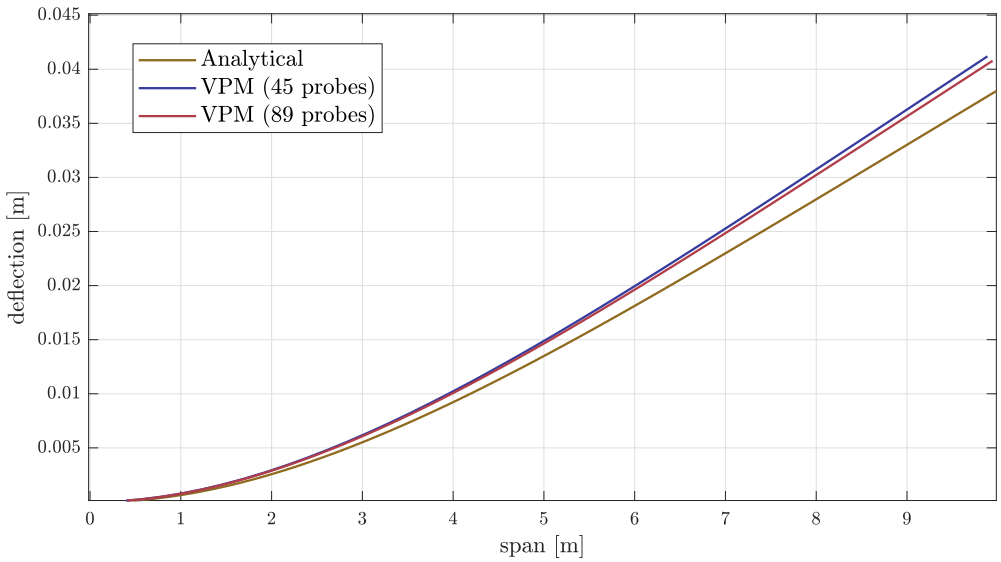

Figure 3.2: Comparison of the deflection distribution of a rectangular half wing between (i) the analytical solution and (ii) the numerical results obtained with VPM and the finite segment method for 45 and 89 probes on the half wingspan.

It can be observed that the numerical results are in line with the analytical solution. The fact that the numerical results overestimate the analytical solution can be explained by the angle of attack distribution (see figure 3.3). The tip losses are slightly underestimated with the solution provided by the flow solver. This implies a larger bending moment on the wing. This tendency decreases with the number of probes on the wing.

Remark

Due to the important stiffness of the system, the damping coefficient must remain low, so that ROBOTRAN is able to solve the system, due to the large time steps performed by the flow solver. The transition period to obtain the steady-state situation is therefore quite long (see figure 3.4).

3.2 Validation 2 : NREL 5-MW wind turbine blade

In the previous section a uniform beam was considered. To ensure the validity of the model to non-uniform cases, the same approach as for the rectangular wing can be implemented for a blade of the NREL 5-MW wind turbine already described in section 2.1.3. The blade flexibility effects in bending and torsion will be treated separately and compared to analytical approximate solutions. The case of flap-wise bending with rotation of the blade will also be analysed.

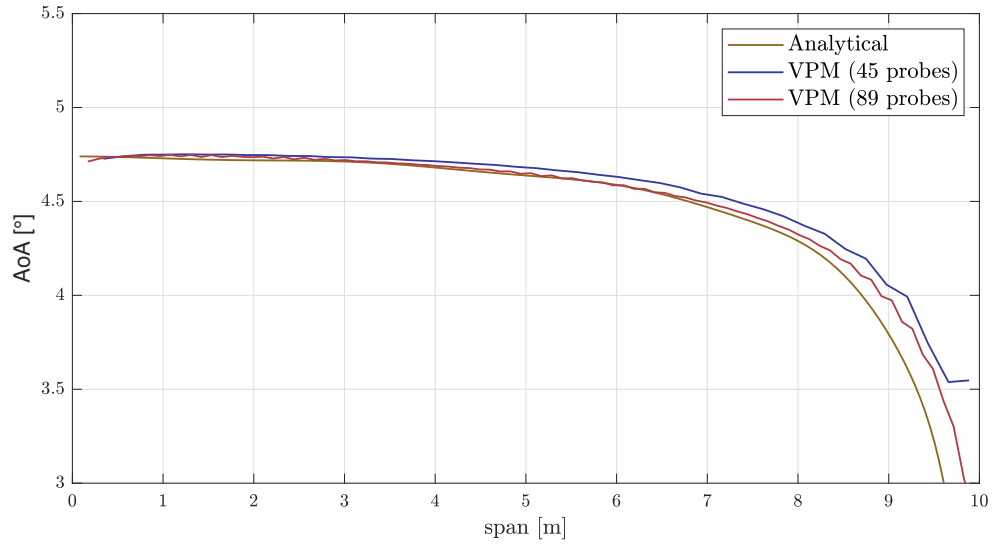

Figure 3.3: Comparison of the angle of attack distribution of a rectangular half wing between (i) the analytical solution and (ii) the numerical results obtained with VPM and the finite segment method for 45 and 89 probes on the half wingspan.

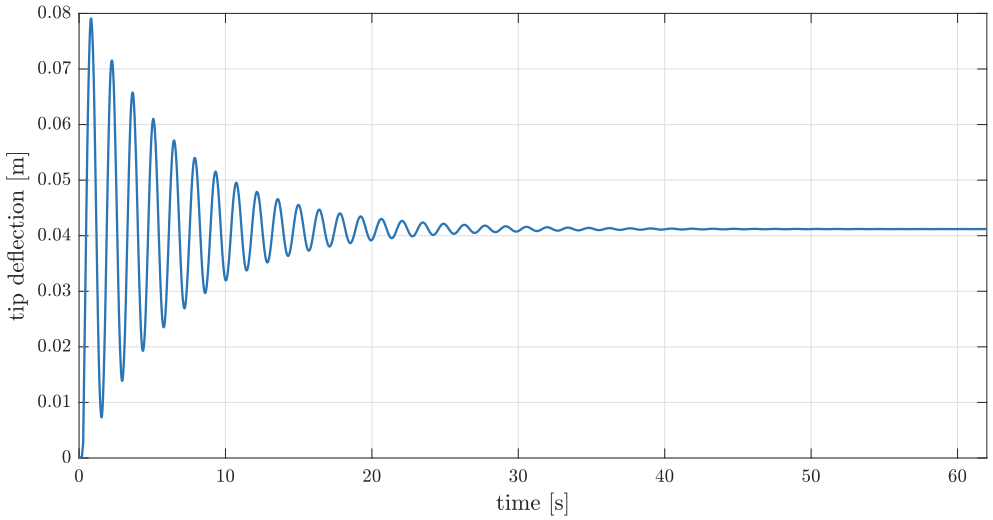

Figure 3.4: Temporal evolution of the tip deflection obtained with 45 probes on the half wingspan.

3.2.1 Testing configuration

Firstly, the non rotating case is treated. One blade of the wind turbine is considered in a pseudo feathered position, i.e., with a pitch control angle of $\theta_c = \pi/2$. The MBS model is similar to the one illustrated in figure 2.7, where the only degrees of freedoms are allowed by the revolute joints between each body constituting the blade that is composed of 12 rigid segments.

Ignoring the induced velocity effects, the angle of attack is the inverse of the geometrical twist angle θ_g (see figure 3.5a), relative to the tip profile. For the NREL 5-MW blade, the twist angle is therefore positive at the root ($\theta_g = 13.3°$) and decreasing along the blade, reaching zero at the tip.

Next, the rotating blade is treated. The pitch control angle is set to $\theta_c = 0$, and also ignoring the induced velocity, the angle of attack is defined by the velocity triangle, as shown

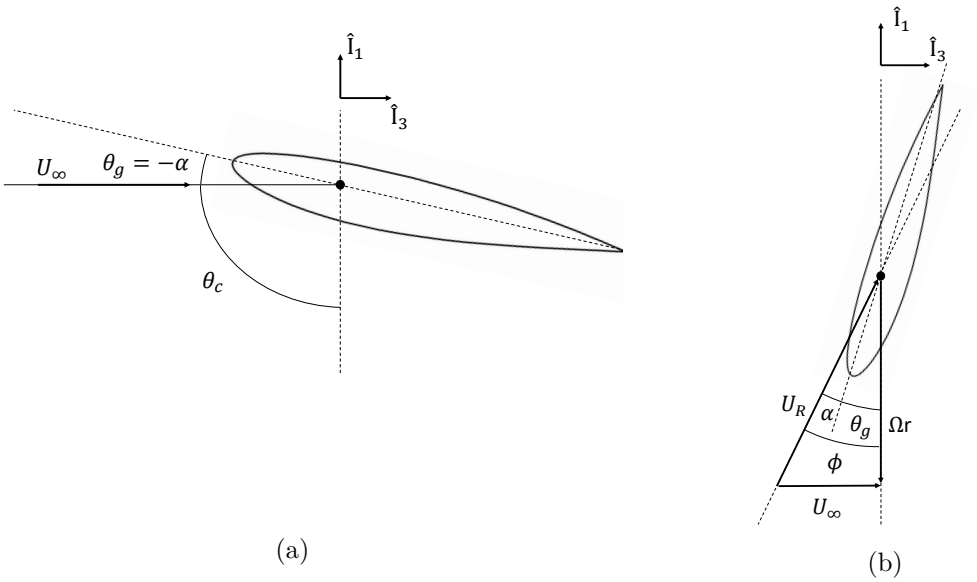

Figure 3.5: Angles and velocity for a section of the blade (a) in feathered position and (b) rotating. The rotation plane of the wind turbine is perpendicular to the $\hat{I}_3$ axis.

in figure 3.5b. The relative velocity U_R and inflow angle ϕ are obtained from the steady inlet wind velocity U_∞ and the rotation velocity at a distance r from the hub Ωr. The angular velocity is fixed to 10 rpm.

In both cases a uniform flow pointing toward the $\hat{I}_3$ direction is applied, corresponding to a wind of velocity $U_\infty = 10[m/s]$.

3.2.2 Analytical solution

The analytical solution is based on the assumed modes theory described in appendix B. The aerodynamic loads are obtained from the blade aerodynamic properties and the flow conditions.

By using the principle of least action to the actions applying on the blade (see Appendix A and B) and without considering damping, the equations of motion are given by

$$\mu(x)\frac{\partial^2 w(x,t)}{\partial t^2} + \frac{\partial^2}{\partial x^2}\Big(EI(x)\frac{\partial^2 w(x,t)}{\partial x^2}\Big) - \frac{\partial}{\partial x}\Big(N(x)\frac{\partial w(x,t)}{\partial x}\Big) = f(x), \tag{3.8}$$

where $w(x,t)$ is the deflection at the position x and time t, $EI(x)$ is the rigidity, $N(x)$ the inertial force due to the rotation velocity and $f(x)$ are the external loads.

The modal analysis using the assumed modes theory provides the mode shapes of the non-uniform beam, e.g., $\tilde{W}_m(x)$ for the mode m (see Appendix B). As only the steady-state case is considered here, a new modal superposition of the form

$$w(x) = \sum_{i=1}^{\infty} P_i \tilde{W}_i(x) \tag{3.9}$$

can be used, where P_i are coefficients to determine. Introducing this decomposition into equation 3.8 yields to

$$\frac{f(x)}{\mu(x)\sum_{i=1}^{\infty} P_i \tilde{W}_i(x)} = Constant = \sum_{i=1}^{\infty} \omega_i^2, \tag{3.10}$$

that can be rewritten such as

$$\sum_{i=1}^{\infty} P_i \mu(x) \omega_i^2 \tilde{W}_i(x) = f(x). \tag{3.11}$$

To obtain the coefficients P_i the latter expression is multiplied by $\tilde{W}_j(x)$ and integrated over the structural domain. By the mode shape orthogonality condition

$$\int_0^L \tilde{W}_i(x) \mu(x) \tilde{W}_j(x) dx = m_i \delta_{ij}, \tag{3.12}$$

with m_i being the modal mass, the coefficients are given by

$$P_j = \frac{1}{m_j \omega_j^2} \int_0^L f(x) \tilde{W}_j(x) dx. \tag{3.13}$$

Finally, the deflection is obtained from equations 3.9 and 3.13, leading to

$$w(x) = \sum_{i=1}^{\infty} \tilde{W}_i(x) \frac{1}{m_i \omega_i} \int_0^L f(x) \tilde{W}_i(x) dx. \tag{3.14}$$

The aerodynamic loads are obtained using the aerodynamic properties data of the blade, given in [19]. To account for the tip-losses, an empirical correction factor is applied to the aerodynamic forces. The correction factor used here is presented in [23]. It is based on the Prandtl tip loss factor and empirically determined from CFD simulations of wind turbine blades

$$F(x) = \begin{cases} (F_{Prandtl}^{0.85}(x) + 0.5)/2 & \text{for } 0.7 \leq x \leq 1, \\ 1 - x(1 - F_{Prandtl}(0.7))/0.7 & \text{for } x < 0.7, \end{cases} \tag{3.15}$$

where x is the adimensional position along the blade. The Prandtl tip loss factor is given by

$$F_{Prandtl}(x) = \frac{2}{\pi} cos^{-1}\Big(exp\Big(-\frac{N_b}{2}\Big(\frac{1-x}{x}\Big)\frac{1}{sin\phi}\Big)\Big), \tag{3.16}$$

with N_b and ϕ being the number of blades and the inflow angle, respectively.

3.2.3 Results

Firstly, the flap-wise and edge-wise deflections, as well as the torsion, are considered separately and for a feathered blade. The deflection and torsion distributions in steady-state, obtained with the finite segment method in the flow solver and compared to the analytical solution, are presented in figure 3.6.

Good agreement between analytical and numerical results can be observed for the flap-wise deflection. For the edge-wise deflection and torsion distribution, both methods provide slightly different values. However, the general shapes are globally consistent.

The differences between both methods are principally due to the effects generated by the induced velocity, that are not taken into account in the analytical solution, except with an empirical correction factor for the tip losses. Hub losses are not taken into account. Indeed, the reduction of the absolute angle of attack generated by the downwash causes a reduction of the drag coefficient, and hence of the edge-wise deflection, and also generates here a larger negative pitching moment. These considerations can be observed in the results, except for torsion at the blade tip.

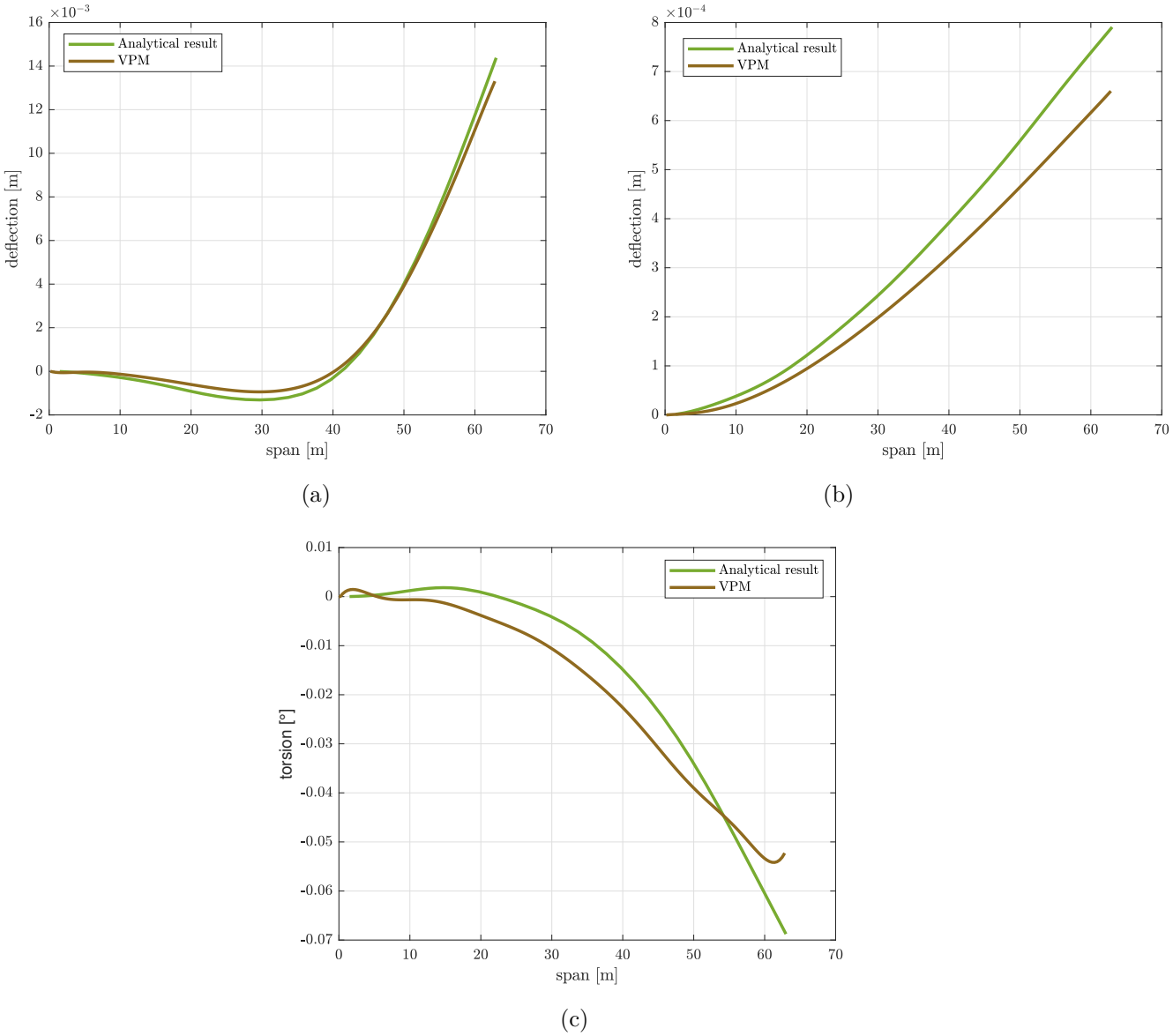

Figure 3.6: Distribution along the blade span of (a) the flap-wise deflection, (b) the lag-wise deflection and (c) the torsion angle relative to the initial twist angle of a feathered NREL 5-MW blade. The results obtained numerically are compared to the analytical solution.

Let us now study the flap-wise deflection of the blade rotating at 10 rpm. The results obtained analytically and numerically are presented in figure 3.7. Once again, the slight differences are due to the fact that, in the analytical solution, the precision of the effects associated to the induced velocity is poor.

It is to note that in this case, the aerodynamic damping plays an important role in the stabilisation of the elastic system, as shown in figure 3.8.

3.3 Application : full NREL 5-MW blade in rotation

Let us consider now the blade of the NREL 5-MW wind turbine with deformations in bending and in torsion allowed. The blade is maintained at an angular velocity of 12.1 rpm and a steady inlet wind velocity of 11.4 m/s is applied. This setup was proposed in [24], as it corresponds to one of the cases reported in [19]. The tip speed ratio in this configuration is

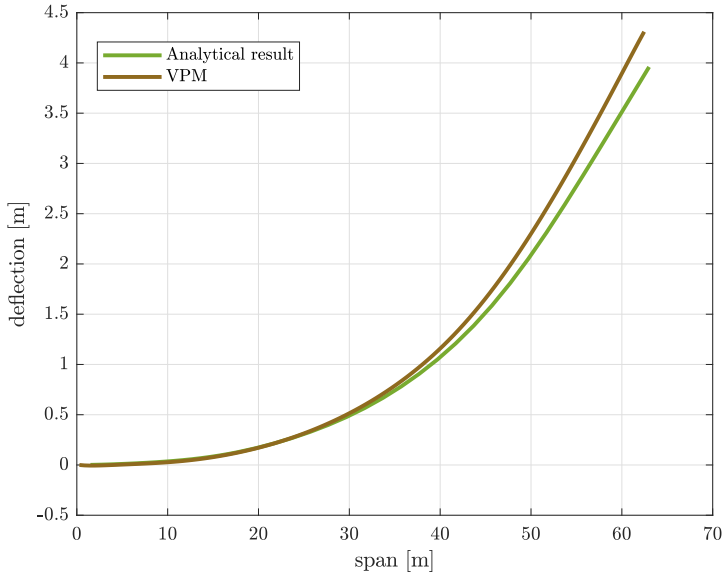

Figure 3.7: Distribution along the blade span of the flap-wise deflection of rotating NREL 5-MW blade. The results obtained numerically are compared to the analytical solution.

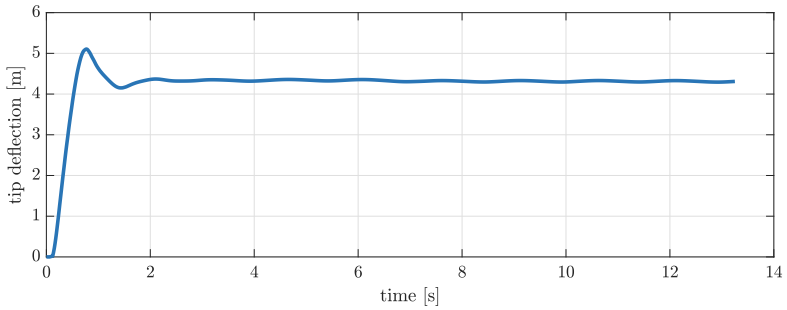

Figure 3.8: Edge-wise deflection distribution of the feathered blade.

$\lambda = \Omega R/U_\infty = 7$, which is the ideal for this wind turbine. In this case, gravity is not neglected. The same simulation was also performed with a rigid blade.

The flexible blade was modelled by using 10 rigid bodies. It is worth noting that for higher number of segments, the simulation performances are lowered due to the very large stiffness of the system.

The temporal evolution of the aerodynamic torque for both rigid and flexible blades is provided in figure 3.9. Large oscillations in the torque provided by the flexible blade are observed. They are caused by the poor stability of the system due to the small damping.

The time history of the flap-wise and edge-wise tip deflection are presented in figure **??**. The flap-wise deflection oscillates between 5.5 and 7 meters, which is significant and consistent with the results provided in [19]. In edge-wise deflection, the effect of gravity contributes to the excitation of the system and due to the low damping, no steady-state is reached.

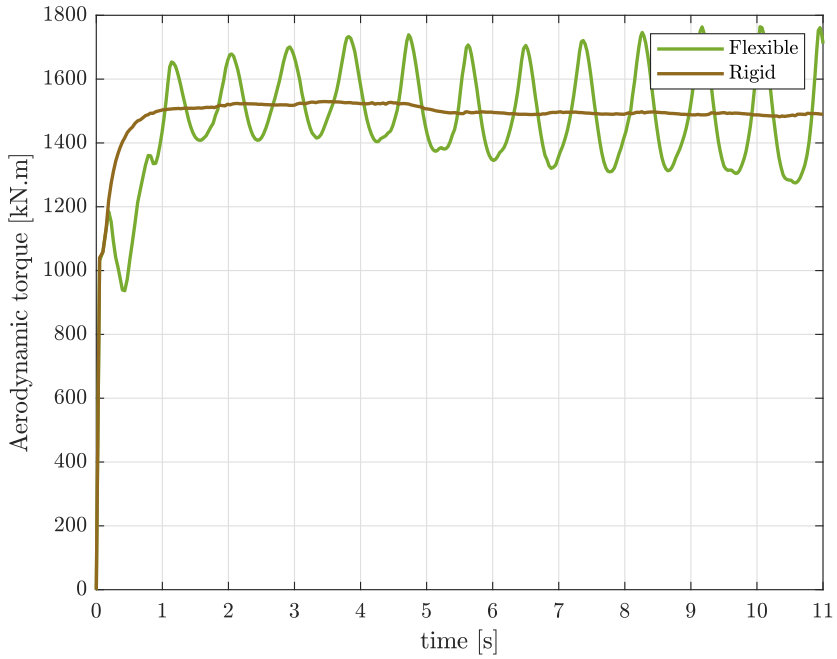

Figure 3.9: Time history of the aerodynamic torque.

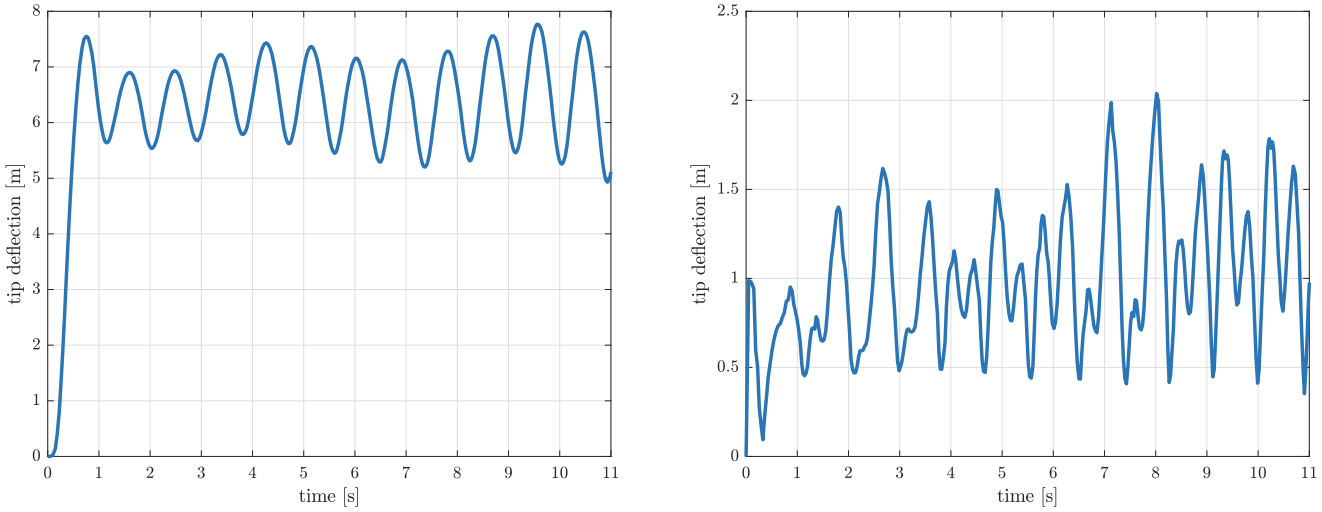

(a) (b)

Figure 3.10: Time history of the flap-wise (a) and of the edge-wise (b) tip deflection.

Conclusion and discussion

This work explored one way of handling the flexibility effects in a CFD solver. The method required a few modifications in the existing tools but did not change the level of complexity of the original solvers. Satisfactory results can be obtained by correctly applying the method, and this in a wide variety of cases.

After a brief description of the numerical tools on which this work is based, i.e., a CFD solver, a Multibody system (MBS) solver and the coupling between both, the finite segment approach in a pure multibody system context was summarized. The spring coefficients determination is based on the Euler-Bernoulli beam theory, and in this context, the material of the body is considered isotropic and in linear elasticity. Several examples demonstrated the effectiveness of this method to model uniform and non uniform flexible slender bodies.

The analysis of the results showed that the number of segments used is a trade-off between the precision of the results and the implementation cost. A number of rigid elements ranging between 10 and 20 seems reasonable. Indeed, as the error decreases at a rate of $\mathcal{O}(1/N)$, using a larger number of segment N would only bring minor benefits to the precision. It was also demonstrated that cantilever beams discretized in finite segments according to Rayleigh's model provide better results than in the Duncan configuration. However, no method could be provided for the damping coefficient, that must be determined empirically.

Modifications were introduced for integrating the finite segment method in the flow solver. To avoid irregularities in the shape of the lifting line due to the discretization in segments, the positions between control points, defined on each segment, were interpolated by combining shape functions. Those shape functions are based on the mode shape of uniform cantilever beams, providing accurate position interpolation for lifting lines having properties close to uniform beams.

Validation steps were performed, comparing the results obtained with the developed method with analytical results. Firstly, the vertical deflection of a uniform rectangular wing, flexible on one half span was studied, and good concordance with the analytical solution was demonstrated. Then, simulations of a non uniform blade were performed, in feathered position and in rotation. Once again, globally good agreement with the analytical solution was showed. Finally a brief comparison between the aerodynamic torque provided by (i) the rigid blade and (ii) the flexible blade was performed. Due to the poor damping, the flexible wing did not reach a steady-state. However, the values of flap-wise and edge-wise deflections were consistent with other simulations.

However, some drawbacks of the method must be highlighted. First of all, it requires a significant user workload to discretize one lifting line into multiple rigid bodies in the graphical editor of ROBOTRAN, and to attribute to each of them a mass, inertia and geometrical properties. The second disadvantage comes from the time steps required by ROBOTRAN to solve very stiff problems. Increasing the number of segments provides better results, however,

it also causes an increase in the stiffness and damping coefficients. For the cases where two direction deflections and torsion are considered, this can lead to the necessity to sharply reduce the time step of the ROBOTRAN integrator, and hence to reduce the simulation performances.

In the future, further improvements could be brought to the method. Firstly, the robustness of the mapping file treatment could be pushed further. Next, the interpolation process could be extended to other configurations, such as restrained and unrestrained beams. The first one can be encountered in vertical axis wind turbines (VAWT), for instance.

Finally, this method could be applied to a larger variety of cases, going from wind turbines to helicopter blades. Simulations for determining the performances, the wake behaviour and also to improve the design could then be obtained with more realism than before.

Bibliography

[1] A wind energy pioneer: Charles f. brush. http://drømstørre.dk/wp-content/wind/miller/windpower%20web/en/pictures/brush.htm. Accessed: 2019-04-17.

[2] Tony Burton, Nick Jenkins, David Sharpe, and Ervin Bossanyi. *Wind Energy Handbook, second edition*. John Wiley Sons Ltd, 2011.

[3] Three gray wind turbine. https://www.pexels.com/photo/alternative-energy-blade-clouds-ecology-243138/. Accessed: 2019-04-17.

[4] Alvaro Cuerva Tejero, José Luis Espino Granado, Óscar López García, José Meseguer Ruiz, and Ángel Sanz Andrés. Teoría de los helicópteros. *Serie de Ingeniería y Técnica Aeroespacial, Universidad Politécnica de Madrid, Madrid, España*, 2009.

[5] Philippe Chatelain, Matthieu Duponcheel, Denis-Gabriel Caprace, Yves Marichal, and Grégoire Winckelmans. Vortex particle-mesh simulations of vertical axis wind turbine flows: from the airfoil performance to the very far wake. *Wind Energy Science*, 2(1):317–328, 2017.

[6] Philippe Chatelain, Alessandro Curioni, Michael Bergdorf, Diego Rossinelli, Wanda Andreoni, and Petros Koumoutsakos. Billion vortex particle direct numerical simulations of aircraft wakes. *Computer Methods in Applied Mechanics and Engineering*, 197(13-16):1296–1304, 2008.

[7] Philippe Chatelain, Stéphane Backaert, Grégoire Winckelmans, and Stefan Kern. Large eddy simulation of wind turbine wakes. *Flow, turbulence and combustion*, 91(3):587–605, 2013.

[8] Philippe Chatelain, Yves Marichal, Matthieu Duponcheel, Maud Moens, and Grégoire Winckelmans. Vortex methods applied to the large eddy simulation of wind turbine flows. *Preprint submitted to Journal of Computational Physics*, 2015.

[9] Philippe Chatelain, Laurent Bricteux, Stéphane Backaert, Grégoire Winckelmans, Stefan Kern, and Petros Koumoutsakos. Vortex particle-mesh methods with immersed lifting lines applied to the large eddy simulation of wind turbine wakes. In *Proc. Wake Conf*, pages 120–125, 2011.

[10] Paul Fisette and Quentin Docquier. Modeling multibody systems with robotran, feb 2019. www.robotran.be.

[11] Jean-Claude Samin and Paul Fisette. *Symbolic Modeling of Multibody Systems*. Kluwer Academic Publishers, 2003.

[12] Paul Fisette, D.A. Johnson, and Jean-Claude Samin. A fully symbolic generation of the equations of motion of multibody systems containing flexible beams. *Computer Methods in Applied Mechanics and Engineering*, 142(1-2):123–152, 1997.

[13] Simon Buffin. Simulation of rotorcraft dynamics through the coupling of a multibody solver and a vortex particle-mesh method. Master's thesis, Ecole polytechnique de Louvain, 2016.

[14] RL Huston and Y Wang. Flexibility effects in multibody systems. In *Computer-Aided Analysis of Rigid and Flexible Mechanical Systems*, pages 351–376. Springer, 1994.

[15] JD Connelly and RL Huston. The dynamics of flexible multibody systems: A finite segment approach—i. theoretical aspects. *Computers & structures*, 50(2):255–258, 1994.

[16] Richard Dale Rocke. Transmission matrices and lumped parameter models for continuous systems. 1966.

[17] Olivier Andre Bauchau and James I Craig. *Structural analysis: with applications to aerospace structures*, volume 163. Springer Science & Business Media, 2009.

[18] S. Miller, T. Soares, and J. Van Weddingen, Y. abd Wendlandt. Modeling flexible bodies with simscape multibody software. Technical report, MathWorks, 2017.

[19] Jason Jonkman, Sandy Butterfield, Walter Musial, and George Scott. Definition of a 5-mw reference wind turbine for offshore system development. Technical report, National Renewable Energy Lab.(NREL), Golden, CO (United States), 2009.

[20] LK Tartibu, Mark Kilfoil, and AJ Van Der Merwe. Vibration analysis of a variable length blade wind turbine. 2012.

[21] Anthony Robert Southey Bramwell, David Balmford, and George Done. *Bramwell's helicopter dynamics*. Elsevier, 2001.

[22] Sudhakar Gantasala. Finite element modelling of the wind turbine blade, feb 2017.

[23] Patrick J Moriarty and A Craig Hansen. Aerodyn theory manual. Technical report, National Renewable Energy Lab., Golden, CO (US), 2005.

[24] Y Bazilevs, M-C Hsu, J Kiendl, R Wüchner, and K-U Bletzinger. 3d simulation of wind turbine rotors at full scale. part ii: Fluid–structure interaction modeling with composite blades. *International Journal for numerical methods in fluids*, 65(1-3):236–253, 2011.

[25] Raymond L Bisplinghoff, Holt Ashley, and Robert L Halfman. *Aeroelasticity*. Addisin-Wesley, 1957.

[26] Grégoire Winckelmans and Philippe Châtealain. Aerodynamics of external flows, 2018. Course notes.

[27] Alvaro Cuerva Tejero, Cristóbal José Gallego Castillo, and Oscar López García. On-shore and off-shore wind turbine systems, 2018. Course notes.

Appendix A

Deformation of uniform cantilever beams

This appendix covers the theoretical aspects of deformations, in bending and torsion, of uniform beams. A beam is a structure in which one dimension is much larger than the other two.

Equation of free vibration in bending

A straight, horizontal beam with one fixed end and a free end submitted to a vertical load will deform into a curve. When the load is removed, the beam will return to its original shape but its inertia will keep the beam in motion, and it will vibrate at its characteristic frequencies.

If we consider a uniform beam, the elastic modulus (E), inertia (I), and cross sectional area (A) are constant along the beam length. The kinetic energy of the blade returning to its original shape is

$$P = \int_0^L \frac{1}{2}\mu\Big(\frac{\partial w}{\partial t}\Big)^2 dx, \tag{A.1}$$

where μ is the mass per unit length and $w = w(x,t)$ the deflection at the position x and time t. On the other hand, the elastic potential energy due to the deformation is expressed as

$$V = \int_0^L \frac{1}{2}EI\Big(\frac{\partial^2 w}{\partial x^2}\Big)^2 dx, \tag{A.2}$$

with E being the elastic modulus and I is the second moment of area of the beam's cross-section. The Euler–Lagrange equation for the action is then given by

$$S = \int_{t_1}^{t_2} (P - V)\mathrm{d}t, \tag{A.3}$$

and by the principle of least action, $\delta S = 0$, the equation of motion for the free vibration is

$$EI\frac{\partial^4 w}{\partial x^4} = -\mu\frac{\partial^2 w}{\partial t^2}. \tag{A.4}$$

This equation is a separable partial differential equation, which has a solution of the form

$$w(x,t) = W(x)T(t), \tag{A.5}$$

where W and T are functions, respectively independent of time and of the position. Substitution of equation A.5 into A.4 yields

$$\frac{EI}{\mu W(x)}\frac{\partial^4 W(x)}{\partial x^4} = -\frac{1}{T(t)}\frac{\partial^2 T(t)}{\partial t^2} = Constant = \omega^2. \tag{A.6}$$

Therefrom, two independent ordinary differential equations are obtained

$$\frac{\partial^2 T}{\partial t^2} + \omega^2 T = 0, \tag{A.7}$$

$$\frac{\partial^4 W}{\partial x^4} - \frac{\omega^2}{a^2} W = 0, \tag{A.8}$$

with $a^2 = EI/\mu$, and the general solution of equation A.8 is given by

$$W(x) = A\ sinh\Big(\sqrt{\frac{\omega}{a}}x\Big) + B\ cosh\Big(\sqrt{\frac{\omega}{a}}x\Big) + C\ sin\Big(\sqrt{\frac{\omega}{a}}x\Big) + D\ cos\Big(\sqrt{\frac{\omega}{a}}x\Big), \tag{A.9}$$

where A, B, C and D are unknown constants.

The quantities ω^2 and $W(x)$ are the eigenvalues and eigenfunctions of the problem and there is an infinite number of pairs of them representing each mode of vibration and the associated frequency.

Equation of free vibration in torsion

The case of torsion can be treated similarly to the bending case. The Saint-Venant torsion theory is hower used, instead of the Euler-Bernoulli theory. The equation of motion for the free vibration is given by

$$GJ\frac{\partial^2 \theta}{\partial x^2} = I_0 \frac{\partial^2 \theta}{\partial t^2}, \tag{A.10}$$

with GJ being the torsional rigidity, θ the angle of twist and I_0 the moment of inertia per unit length about the center of twist. This equation is also separable and can be solved by introducing the separation

$$\theta(x,t) = \Theta(x)T(t), \tag{A.11}$$

providing two independent ordinary differential equations

$$\frac{\partial^2 T}{\partial t^2} + \omega^2 T = 0, \tag{A.12}$$

$$\frac{\partial^2 \Theta}{\partial x^2} - \frac{\omega^2}{a^2}\Theta = 0, \tag{A.13}$$

where $a^2 = GJ/I_0$. The general solution of equation A.13 is

$$\Theta(x) = Asin\Big(\frac{\omega}{a}x\Big) + Dcos\Big(\frac{\omega}{a}x\Big). \tag{A.14}$$

The quantities ω^2 and $\Theta(x)$ are the eigenvalues and eigenfunctions of the problem and there is an infinite number of pairs of them representing each mode of vibration and the associated frequency.

Cantilever beam

In the case of a cantilever beam of length L clamped in $x = 0$, the boundary conditions in bending are

$$W(0) = 0,\ \frac{\partial W(0)}{\partial x} = 0,\ \frac{\partial^2 W(L)}{\partial x^2} = 0,\ \frac{\partial^3 W(L)}{\partial x^3} = 0, \tag{A.15}$$

that yield two equations

$$\Big(cosh\Big(\sqrt{\frac{\omega}{a}}L\Big) + cos\Big(\sqrt{\frac{\omega}{a}}L\Big)\Big)A + \Big(sinh\Big(\sqrt{\frac{\omega}{a}}L\Big) - sin\Big(\sqrt{\frac{\omega}{a}}L\Big)\Big)B = 0, \tag{A.16}$$

$$\Big(sinh\Big(\sqrt{\frac{\omega}{a}}L\Big) + sin\Big(\sqrt{\frac{\omega}{a}}L\Big)\Big)A + \Big(cosh\Big(\sqrt{\frac{\omega}{a}}L\Big) + cos\Big(\sqrt{\frac{\omega}{a}}L\Big)\Big)B = 0. \tag{A.17}$$

By setting the determinant of this system to zero, the following expression for the frequency ω is obtained

$$cos\Big(\sqrt{\frac{\omega}{a}}L\Big)cosh\Big(\sqrt{\frac{\omega}{a}}L\Big) = -1. \tag{A.18}$$

The natural mode shapes corresponding to the frequencies are finally given by

$$W_n(x) = B\Bigg[\Bigg(\frac{sin\Big(\sqrt{\frac{\omega}{a}}L\Big) - sinh\Big(\sqrt{\frac{\omega}{a}}L\Big)}{cosh\Big(\sqrt{\frac{\omega}{a}}L\Big) + cos\Big(\sqrt{\frac{\omega}{a}}L\Big)}\Bigg)\Big(sinh\Big(\sqrt{\frac{\omega}{a}}x\Big) - sin\Big(\sqrt{\frac{\omega}{a}}x\Big)\Big) + \Big(cosh\Big(\sqrt{\frac{\omega}{a}}x\Big) - cos\Big(\sqrt{\frac{\omega}{a}}x\Big)\Big)\Bigg], \tag{A.19}$$

where the constant B is arbitrary, and those functions are orthogonal between them, with respect to a weighting function.

In torsion, the boundary conditions on $\Theta(x)$ are

$$\Theta(0) = 0, \ \frac{\partial\Theta(L)}{\partial x} = 0, \tag{A.20}$$

that yields to the following expression for the frequency

$$cos\Big(\frac{\omega}{a}L\Big) = 0. \tag{A.21}$$

The natural mode shapes corresponding to the frequencies are given by

$$\Theta_n(x) = A\ sin\frac{n\pi}{2L}x, \qquad (\text{n} = 1,\ 3,\ 5,...,\ \infty). \tag{A.22}$$

Appendix B

Assumed mode method for the bending of a non-uniform rotating blade

The assumed mode procedure consists in assuming a finite series of approximation functions [21], i.e., the deflection is given by

$$w(x,t) = \sum_{k=1}^{n} W_k(x)\phi_k(t), \tag{B.1}$$

where W_k are functions satisfying the geometrical boundary conditions (equation A.19 for example) and ϕ_k are generalized coordinates. As in appendix A, the structural dynamics equations of the elastic blades stem from the principle of least action of the different types of energy of the blade. However, we consider here a non uniform rotating blade submitted to external forces.

The kinetic energy can be expressed as

$$P = \int_0^L \frac{1}{2}\mu(x)\Big(\frac{\partial w}{\partial t}\Big)^2 dx, \tag{B.2}$$

and using expression B.1, it can be written as

$$P = \frac{1}{2}\sum_{k=1}^{n}\sum_{l=1}^{n} M_{kl}\frac{\mathrm{d}\phi_k}{\mathrm{d}t}\frac{\mathrm{d}\phi_l}{\mathrm{d}t}, \tag{B.3}$$

where M_{kl} are the elements of the called mass matrix and that depend on the mass distribution $\mu(x)$ of the blade

$$M_{kl} = \int_0^L W_k(x)\mu(x)W_l(x)\mathrm{d}x. \tag{B.4}$$

Similarly, the elastic potential energy due to the deformation is expressed as

$$V_s = \int_0^L \frac{1}{2}EI(x)\Big(\frac{\partial^2 w}{\partial x^2}\Big)^2 dx \tag{B.5}$$

$$= \frac{1}{2}\sum_{k=1}^{n}\sum_{l=1}^{n} K_{s,kl}\phi_k\phi_l, \tag{B.6}$$

with $K_{s,kl}$ being the elements of the stiffness matrix accounting for the structural effects

$$K_{s,kl} = \int_0^L \frac{\mathrm{d}^2 W_k}{\mathrm{d}x^2}EI(x)\frac{\mathrm{d}^2 W_l}{\mathrm{d}x^2}\mathrm{d}x, \tag{B.7}$$

and also the potential energy due to the centrifugal effect of the blade in rotation is

$$V_c = \int_0^L \frac{1}{2} N(x) \Big(\frac{\partial w}{\partial x}\Big)^2 \mathrm{d}x \tag{B.8}$$

$$= \frac{1}{2} \sum_{k=1}^{n} \sum_{l=1}^{n} K_{c,kl} \phi_k \phi_l, \tag{B.9}$$

where $K_{c,kl}$ are the elements of the stiffness matrix accounting for the centrifugal effects

$$K_{c,kl} = \int_0^L \frac{\mathrm{d}W_k}{\mathrm{d}x} EI(x) \frac{\mathrm{d}W_l}{\mathrm{d}x} \mathrm{d}x, \tag{B.10}$$

and $N(x)$ is the inertial force due to the rotation velocity Ω

$$N(x) = \int_x^L \mu(\xi) \Omega^2 \xi \mathrm{d}\xi. \tag{B.11}$$

Modal analysis

The equations of motion are obtained by using the equations of Lagrange associated to the generalized coordinates ϕ, defining the Lagrangian as $L = T - V_s - V_c$

$$\frac{\mathrm{d}}{\mathrm{d}t}\Big(\frac{\partial L}{\partial \dot{\phi}_m}\Big) - \frac{\partial L}{\partial \phi_m} = 0, \tag{B.12}$$

with $m = 1, \ldots, n$.

One then obtains the system of ordinary differential equations

$$\sum_{l=1}^{n} M_{ml} \frac{\mathrm{d}^2 \phi_l}{\mathrm{d}t^2} + \sum_{l=1}^{n} (K_{s,ml} + K_{c,ml}) \phi_l = 0. \tag{B.13}$$

By imposing a harmonic movement condition to the generalized coordinates, the eigenvalue problem is obtained

$$(\omega^2 [\mathbf{M}] - [\mathbf{K}]) \cdot \mathbf{A} = \mathbf{0}, \tag{B.14}$$

with ω the natural frequencies, $[\mathbf{M}]$ the mass matrix, $[\mathbf{K}] = [\mathbf{K}_s] + [\mathbf{K}_c]$ is the stiffness matrix and $\mathbf{A}$ are the eigenvectors.

Finally, the approximated natural mode shape of vibration associated to the mode m $\tilde{W}_m(x)$ is given by

$$\tilde{W}_m(x) = \sum_{k=1}^{n} A_{km} W_k(x). \tag{B.15}$$

UNIVERSITÉ CATHOLIQUE DE LOUVAIN
École polytechnique de Louvain
Rue Archimède, 1 bte L6.11.01, 1348 Louvain-la-Neuve, Belgique | **www.uclouvain.be/epl**